Shear-Relative Asymmetric Kinematic Characteristics of Intensifying Hurricanes as Observed by Airborne Doppler Radar

UDAI SHIMADA,[a] PAUL D. REASOR,[b] ROBERT F. ROGERS,[b] MICHAEL S. FISCHER,[b,c] FRANK D. MARKS,[b]
JONATHAN A. ZAWISLAK,[b,c] AND JUN A. ZHANG[b,c]

[a] *Meteorological Research Institute, Tsukuba, Ibaraki, Japan*
[b] *NOAA/AOML/Hurricane Research Division, Miami, Florida*
[c] *University of Miami/Cooperative Institute for Marine and Atmospheric Studies, Miami, Florida*

(Manuscript received 13 December 2022, in final form 3 December 2023, accepted 8 December 2023)

ABSTRACT: While recent observational studies of intensifying (IN) versus steady-state (SS) hurricanes have noted several differences in their axisymmetric and asymmetric structures, there remain gaps in the characterization of these differences in a fully three-dimensional framework. To address these limitations, this study investigates differences in the shear-relative asymmetric structure between IN and SS hurricanes using airborne Doppler radar data from a dataset covering an extended period of time. Statistics from individual cases show that IN cases are characterized by peak wavenumber-1 ascent concentrated in the upshear-left (USL) quadrant at ~12-km height, consistent with previous studies. Moderate updrafts (2–6 m s^{-1}) occur more frequently in the downshear eyewall for IN cases than for SS cases, likely leading to a higher frequency of moderate to strong updrafts USL above 9-km height. Composites of IN cases show that low-level outflow from the eye region associated with maximum wavenumber-1 vorticity inside the radius of maximum wind (RMW) in the downshear-left quadrant converges with low-level inflow outside the RMW, forming a stronger local secondary circulation in the downshear eyewall than SS cases. The vigorous eyewall convection of IN cases produces a net vertical mass flux increasing with height up to ~5 km and then is almost constant up to 10 km, whereas the net vertical mass flux of SS cases decreases with height above 4 km. Strong USL upper-level ascent provides greater potential for the vertical development of the hurricane vortex, which is argued to be favorable for continued intensification in shear environments.

KEYWORDS: Intensification; Tropical cyclones; Aircraft observations

1. Introduction

Understanding the relationship between tropical cyclone (TC) structure and intensity change is essential to elucidate intensification mechanisms and improve the accuracy of intensity forecasts. The intensity of TCs changes through internal processes closely related to TC structure as well as external influences such as environmental conditions (e.g., Emanuel 1986; Kaplan and DeMaria 2003; Nolan et al. 2007; Pendergrass and Willoughby 2009; Rogers et al. 2013; Hendricks et al. 2019; Shimada 2022).

Environmental vertical wind shear is one of the main factors that influence TC structure (e.g., Frank and Ritchie 1999; Chen et al. 2006; Reasor et al. 2013). TCs in shear have a quasi-stationary wavenumber-1 (WN-1) asymmetry (Frank and Ritchie 2001; Black et al. 2002; Braun and Wu 2007; Riemer et al. 2010; Reasor et al. 2013; DeHart et al. 2014). Black et al. (2002) described the shear-induced convective asymmetry based on two hurricanes. Convective cells form near the downshear eyewall as a result of shear forcing. They develop as they rotate around the eye with maximum rainfall in the downshear-left quadrant (DSL). Descent driven by precipitation and induced by shear, and ascent accelerated by water unloading were observed in the lower and upper troposphere upshear, respectively.

With the availability of aircraft observations of the inner-core structure of tropical cyclones (TCs) spanning several decades, an emphasis in the research community has been placed in recent years on identifying possible relationships between TC inner-core structure and intensity change. Previous studies have characterized differences in the kinematic structure of intensifying (IN) versus steady-state (SS) hurricanes using airborne Doppler radar observations (e.g., Rogers et al. 2013; Hazelton et al. 2015; Wadler et al. 2018). Within an axisymmetric framework, Rogers et al. (2013) showed that vigorous deep convection occurred more frequently inside the radius of maximum wind (RMW) for IN cases than for SS cases. When fields were oriented relative to the deep-layer shear direction, they also found that IN cases exhibited stronger composite-mean mid- to upper-tropospheric ascent within the upshear-left (USL) eyewall than their SS counterpart. Consistent with this finding, Rogers et al. (2016) showed that strong updrafts persisted at upper levels USL during the rapid intensification (RI) of Hurricane Edouard (2014). More recently, Wadler et al. (2018) compared characteristics of deep convection for the same two intensity change groupings. They found a key characteristic of IN cases was a greater frequency of stronger updrafts, peaking at a higher altitude (>10 km), with higher echo tops USL compared with SS cases. The correlation between strong USL upper-level updrafts and intensification was interpreted in terms of an enhancement of

---

Supplemental information related to this paper is available at the Journals Online website: https://doi.org/10.1175/MWR-D-22-0340.s1.

Corresponding author: Udai Shimada, ushimada@mri-jma.go.jp

DOI: 10.1175/MWR-D-22-0340.1

symmetric diabatic heating (Wadler et al. 2018). A similar result was found by Hazelton et al. (2015), who focused on the slope of the 20-dBZ reflectivity surface, relative to the slope of the angular momentum surface, on the inner side of the eyewall. They showed that the reflectivity slope for IN cases was more upright than the angular momentum slope USL, while the reverse was true for SS cases. This feature implies that IN cases have more intense convective precipitation USL than SS cases. Consistent with these airborne-radar-based observations, Tao and Jiang (2015) showed from satellite observations that greater frequencies of moderately to very deep precipitation (i.e., a 20-dBZ echo-top height > 10 km) USL are associated with greater TC intensification rates. In particular, Tao and Jiang (2015) demonstrated the largest composite frequencies of moderately to very deep precipitation in the USL quadrant occur in the "RI continuing" group, which signals the importance of USL ascent for TC intensification in relatively strong storms. Because the modulation of microphysical fields by USL updrafts can be easily detected via remote sensing, intensity forecasts may be aided by the incorporation of this indirect information on diabatic heating symmetry.

Other studies, however, have shown that maximum wind spinup occurs in the boundary layer, where TC intensity is actually defined. Strong convection plays a role such that if the eyewall mass flux exceeds that required to ventilate the mass exiting the top of the boundary layer, air is drawn inward above the boundary layer and, through convergence of angular momentum, the tangential flow is spun up there (e.g., Smith and Montgomery 2015; Kilroy et al. 2016; Montgomery and Smith 2017; Smith and Wang 2018; Smith et al. 2021; Zhang et al. 2023). In the context of simulated TCs, Kilroy et al. (2016) demonstrated that positive vertical mass flux integrated over the inner core (radii < 200 km) at 6-km height exceeds that at 1.5-km height during intensification. Smith et al. (2021) utilized similar levels of vertical mass flux in the definition of a ventilation diagnostic for interpreting intensification and decay phases of a simulated hurricane. Thus, although previous observation-based studies have identified strong updrafts at upper levels ($>$10 km) as being a statistically significant, distinguishing feature of IN storms, the aforementioned boundary layer and ventilation pathway would suggest that the intensification process is strongly controlled by processes within the lower to middle troposphere. To bridge this gap between the upper-level, observation-based findings of Wadler et al. (2018) and the simulation-based studies of lower-level intensification processes, a comprehensive observational examination of three-dimensional shear-relative asymmetric kinematic characteristics in the eyewall region of IN hurricanes is needed.

This study aims to characterize the shear-relative asymmetric kinematic structure of IN hurricanes in comparison with SS hurricanes using an extended database of observed hurricane-strength storms that incorporates more cases than those used in Rogers et al. (2013) and Wadler et al. (2018). The motivation here of comparing IN cases with SS cases is not to explain the cause of the difference in intensification rate but to diagnose structural differences as a function of intensification rate. The present study will show that the aforementioned upper-level ascent asymmetry is tied to the kinematic structure at lower levels, where recent intensification theories have focused. Specifically, this study analyzes airborne Doppler radar data obtained from NOAA WP-3D (P-3) missions from 1997 to 2019 using a composite approach to look at differences in quasi-stationary eyewall asymmetries between IN and SS cases. An emphasis is placed on characterizing differences in the asymmetric structure in a fully three-dimensional framework, to bridge the gap between upper-level ascent and lower-level processes described above. Note that this composite approach limits the capability to find the exact cause and effect of asymmetric structure and intensification that would otherwise be possible through an observational case study with time evolution or with numerical model output. Here, we aim to characterize how the asymmetric kinematic characteristics of IN hurricanes significantly differ from SS hurricanes. This approach provides new insight into the relationship between eyewall convection and intensification for hurricane-strength storms in shear and points toward possible causal mechanisms that are recommended to be explored in future research.

The rest of the paper consists of five sections. First, we provide information on data and methodology in section 2. Next, we confirm prior work highlighting differences in upper-level USL updraft characteristics between IN and SS hurricanes using a larger database than previous studies in section 3. Then we investigate differences in the axisymmetric and asymmetric kinematic structures between IN and SS hurricanes in section 4. We argue the relationship between asymmetric eyewall convection and intensification based on the results in section 5. Finally, we present our conclusions in section 6.

2. Data and methodology

a. Data

This study utilizes X-band tail-Doppler radar (TDR) analysis data obtained from NOAA P-3 missions from 1997 to 2019. The period of data used in this study is larger than that of most previous TDR composite studies (e.g., Rogers et al. 2013; Hazelton et al. 2015; Wadler et al. 2018). Accordingly, the number of TC samples has increased. Also, the TDR was upgraded to a dual-transmitting solid-state system in 2017, which increased the sensitivity of upper-level observations (Fischer et al. 2022). These factors allow for analyzing features at upper levels. During each mission, an intensive observing period (IOP) consists of multiple radial passes through the TC center. Here, one radial pass is defined as an inbound plus outbound radial leg through the center of the storm. The analysis data are archived by each radial pass. They include three-dimensional wind velocity and radar reflectivity on a Cartesian grid with 2-km horizontal and 0.5-km vertical resolution from 0.5- to 18-km height, centered on the flight-level fix determined by the aircraft flight crew or, in limited cases where a fix was not reported, using circulation center estimates following the method of Willoughby and Chelmow (1982). The three-dimensional wind velocity is retrieved through a variational method (Reasor et al. 2009).

Quality control was introduced to remove the data with high vertical velocity (w) despite low reflectivity: $w \geq 2.5$ m s^{-1} despite reflectivity ≤ 10 dBZ below 10.5-km height and $w \geq 3.0$ m s^{-1} despite reflectivity ≤ 5 dBZ above 10-km height. For most years of the dataset, the two P-3s were equipped with different X-band radar systems in a given hurricane season [see Fischer et al. (2022) for additional details]. Some discrepancies were identified between reflectivity values observed by the two radars, and thus a calibration correction was applied (see the appendix).

In addition to the TDR dataset, Statistical Hurricane Intensity Prediction Scheme (SHIPS; DeMaria and Kaplan 1994, 1999; DeMaria et al. 2005) developmental data (SHIPS 2020) are used to obtain information on storm location, best track intensity (Vm), and environmental conditions for TCs at 6-h intervals. The SHIPS deep-layer (850–200 hPa) shear parameter, which is the mean shear within 500 km from the center with a vortex removed, is used to characterize the shear-relative asymmetric structure. Because no shear calculation is perfect, the results might change when using a different shear definition due to uncertainties in estimating "environmental" shear.

b. *Definitions*

This study limits TC intensity to hurricane-strength storms from 80 to 135 kt (~41–69 m s^{-1}). TCs within this intensity range generally have eyewalls (e.g., Vigh et al. 2012) and tend to be observed with sufficient radar coverage along the eyewall, in particular, at upper levels (Fischer et al. 2022). The synoptic time (0000, 0600, 1200, and 1800 UTC) closest to the middle of an aircraft mission is defined as $t = 0$ h. Intensity changes are defined as ±6 h from $t = 0$ h (i.e., maximum wind changes over a 12-h duration from the best track dataset, ΔVm). IN storms are defined as $\Delta\text{Vm} \geq 10$ kt, and SS storms as $|\Delta\text{Vm}| \leq 5$ kt (1 kt ≈ 0.51 m s^{-1}). However, cases that experienced both intensification and weakening during 12 h and IN cases that stopped intensification at $t = 0$ h are not included. This restriction was implemented to focus on cases experiencing persistent intensity change episodes, rather than short-lived intensity fluctuations, which may be caused by influences outside the scope of this analysis, such as eyewall replacement cycles (e.g., Sitkowski et al. 2011). In the end, 27 IN and 33 SS missions were selected for this study (Table 1). Out of the selected missions, 15 IN missions (56%) were sampled after the upgrade to the radar in 2017, and 20 IN missions (74%) had RMWs less than 40 km, whereas only six SS missions (18%) were sampled after the upgrade and 16 SS missions (48%) had RMWs less than 40 km. These differences resulted in differences in radar coverage at upper levels and in the outer region between IN and SS cases (not shown). Although we only analyze cases with adequate radar coverage at 12-km height or higher for a composite analysis in section 4, the SS composite still has poorer coverage at upper levels than the IN composite. This is a caveat to the composite analysis. We, however, did not find any serious impact on the interpretation of results, except that the area of comparison between IN and SS cases would be limited.

c. *Analysis methods*

In this study, two sets of TDR analysis data are used: swath data (i.e., radial pass data) and merged data from all radial passes during an IOP [usually 3–4 h, see details in Rogers et al. (2013)]. While each swath provides a glimpse of the TC kinematic structure over a relatively short (~45 min) time period, merged analyses give approximately time-mean fields during the 3–4 h of an IOP.

For each swath analysis, storm-relative wind vectors were computed by removing the storm translation from retrieved wind vectors. The storm translation is calculated by a 12-h centered difference in the best track position. Kinematic quantities such as vorticity and divergence were calculated on a Cartesian grid.

A merged set of fields was computed for each IOP using the swath analyses. The center position that maximizes the azimuthal mean tangential wind speed at 2-km height was determined in the merged wind field (e.g., Marks et al. 1992). Then, merged analyses with a Cartesian grid were converted into a TC-centered, shear-relative cylindrical coordinate system, and azimuthal means were computed. The azimuthal-mean value was not calculated if a data gap was greater than 120° in the azimuthal direction at a given radius. The RMW was obtained from the resulting azimuthal mean, and the radial dimension was scaled by the 2-km RMW to account for differences in storm size ($R^* = r/\text{RMW}$, where r is the radius from the center). In general, merged fields smooth transient small-scale fields (in particular, the vertical velocity field) observed in radial passes, but the degree of the smoothing depends on the number of radial passes at a given point during an IOP. The original small-scale convective structure tends not to be smoothed if the number of radial passes is less than 3.

There are two sets of composites in this study. One is from merged analyses for an azimuthal-mean composite. In this composite, each IOP contributes equally to the composite. A minimum of eight missions, about half the number of IN or SS cases in the composite analysis (18 or 15, respectively, see section 4), was required to make the composite field at any given location in radius–height space. The other type of composite uses swath data to examine the eyewall in azimuth–height space and to construct shear-relative quadrant means. In this swath composite, convective structure from each radial pass contributes equally to the composite. The RMW obtained from merged analyses and the dynamic center were used when the radial pass data were converted into a TC-centered, shear-relative cylindrical coordinate system. A minimum number of 11 individual radial passes (about one-sixth the number of IN or SS radial passes, 63 or 59, respectively, see section 4) were required for the swath composite at any given location. This minimum number was determined by the fact that one radial pass generally covers only about one-third of the eyewall [see Fig. 1 of Rogers et al. (2013)], in addition to about half the number of IN or SS radial passes.

We calculated contoured frequency by altitude diagrams (CFADs; Yuter and Houze 1995) of w and total vertical mass flux in the eyewall region using swath data. Because the

TABLE 1. Summary of the TCs used in this study. The circle and hyphen in the "Composite analysis" column denote the cases selected and not selected for the composite analysis in section 4, respectively; $\overline{v}_{\max}$ denotes the maximum azimuthal-mean tangential wind speed.

Storm name	Composite analysis	Year	Date	Center time of each IOP (UTC)	No. of passes	Best track Vm (kt)	Best track Vm change per 12 h (kt)	$\overline{v}_{\max}$ at 2-km height (m s^{-1})	RMW at 2-km height (km)
					IN				
Guillermo	○	1997	2 Aug	2022	2	105	25	50.9	33
Guillermo	○	1997	2 Aug	1915	2	105	25	51.4	32
Ivan	○	2004	7 Sep	1738	4	105	15	49.1	17
Rita	—	2005	20 Sep	1707	3	85	25	40.1	47
Gustav	○	2008	30 Aug	1110	3	110	40	50.5	36
Ike	—	2008	10 Sep	1155	5	80	15	35.4	183
Paloma	○	2008	7 Nov	1847	5	80	25	42.9	27
Bill	—	2009	18 Aug	2359	3	105	15	49.1	53
Earl	—	2010	29 Aug	2246	4	85	20	35.4	45
Earl	○	2010	30 Aug	1224	3	105	20	44.8	35
Earl	—	2010	1 Sep	1146	2	110	10	51.4	45
Matthew	○	2016	30 Sep	1711	2	120	45	50.1	22
Harvey	○	2017	25 Aug	0518	3	90	15	40.4	22
Harvey	○	2017	25 Aug	1730	2	105	20	51.8	25
Irma	—	2017	4 Sep	1106	4	110	10	49.5	20
Irma	○	2017	4 Sep	2352	4	125	20	56.6	30
Lane	—	2018	20 Aug	1823	3	110	10	48.6	22
Lane	○	2018	21 Aug	0610	4	120	15	56.5	22
Michael	○	2018	9 Oct	1141	5	90	15	40.3	41
Michael	○	2018	9 Oct	2447	5	110	20	50.9	29
Michael	○	2018	10 Oct	1053	3	125	15	57.1	24
Dorian	—	2019	29 Aug	2454	3	80	15	37.9	19
Dorian	—	2019	30 Aug	1328	4	95	10	44.4	23
Dorian	○	2019	30 Aug	2402	3	115	20	56.6	15
Dorian	○	2019	31 Aug	1236	5	125	10	59.0	17
Dorian	○	2019	31 Aug	2430	4	135	15	64.1	17
Lorenzo	○	2019	28 Sep	1855	4	115	25	52.7	47
					SS				
Guillermo	○	1997	3 Aug	2127	5	130	0	64.1	27
Fabian	○	2003	3 Sep	1957	5	110	5	53.3	24
Isabel	—	2003	16 Sep	1350	2	95	−5	45.6	104
Frances	—	2004	1 Sep	1834	3	120	0	60.5	39
Frances	—	2004	4 Sep	1949	2	90	5	46.7	74
Ivan	—	2004	12 Sep	1312	3	135	−5	56.7	57
Ivan	—	2004	14 Sep	2100	4	120	0	66.0	46
Ivan	○	2004	14 Sep	2353	6	120	0	64.3	46
Ivan	—	2004	15 Sep	2054	4	115	−5	55.4	40
Jeanne	—	2004	24 Sep	1844	3	85	5	40.0	63
Jeanne	—	2004	24 Sep	1900	3	85	5	39.7	66
Katrina	—	2005	27 Aug	1829	3	100	0	46.8	54
Wilma	○	2005	20 Oct	2009	3	130	0	65.8	37
Gustav	○	2008	31 Aug	2348	7	95	0	44.4	40
Ike	—	2008	10 Sep	2402	5	85	0	40.2	77
Ike	—	2008	11 Sep	1229	5	85	0	40.5	69
Ike	—	2008	12 Sep	1455	4	95	5	49.5	84
Bill	—	2009	19 Aug	2334	3	115	0	54.7	39
Earl	○	2010	30 Aug	2226	3	115	0	53.3	23
Arthur	—	2014	3 Jul	2038	1	80	5	36.3	36
Edouard	○	2014	15 Sep	1733	2	95	5	47.3	37
Edouard	○	2014	15 Sep	1618	2	95	5	49.4	38
Edouard	—	2014	17 Sep	1456	2	80	−5	38.7	86
Gonzalo	—	2014	15 Oct	1425	1	115	−5	46.0	13
Matthew	○	2016	1 Oct	1725	2	130	−5	56.2	13
Matthew	—	2016	5 Oct	1113	3	105	−5	47.0	31

TABLE 1. (*Continued*)

Storm name	Composite analysis	Year	Date	Center time of each IOP (UTC)	No. of passes	Best track Vm (kt)	Best track Vm change per 12 h (kt)	$\overline{v}_{\max}$ at 2-km height (m s^{-1})	RMW at 2-km height (km)
Matthew	○	2016	5 Oct	2122	3	105	5	44.8	29
Irma	○	2017	3 Sep	2239	3	100	5	46.9	26
Irma	—	2017	8 Sep	1132	4	135	5	64.1	46
Maria	○	2017	23 Sep	2126	3	100	−5	44.9	34
Maria	○	2017	24 Sep	0848	4	95	−5	47.9	49
Lane	○	2018	20 Aug	0616	3	105	0	47.2	20
Dorian	○	2019	5 Sep	1206	8	100	−5	45.1	49

RMW differs between cases, the variable RMWs would give more weight to larger RMW storms in the CFADs. To avoid this, the swath data were bilinearly interpolated into R^* radial and azimuthal grid spacing of 0.02° and ~0.7°, respectively. Whereas this resolution is much higher than the original one in the inner core, the converted data maintain the original resolution for large RMW storms and in the outer region. The CFAD of w was constructed from the interpolated gridpoint data. Mass flux was also calculated using the interpolated gridpoint data, assuming the same RMW so that the difference in the RMW between cases does not affect the magnitude of mass flux, and the density from Jordan's (1958) standard tropical Atlantic atmospheric profile. Then, the mass flux was summed up to give the total mass flux of IN or SS groups and normalized by the maximum total mass flux value. Previous studies (e.g., Hence and Houze 2008; Didlake and Houze 2013; Rogers et al. 2013, 2020) have applied the Jordan (1958) sounding to construct vertical mass flux CFADs, and we estimated little influence of the use of the climatological density profile on the normalized mass flux (not shown).

d. Statistical tests

To compare composite mean fields between IN and SS cases, we performed the Wilcoxon–Mann–Whitney rank-sum test, which is a nonparametric test, with a test level of α = 0.05 (i.e., the 95% significance level). As Wilks (2016) pointed out, it is almost certain that for multiple null hypothesis tests like statistical tests at many spatial grid points, at least one of the true null hypotheses is erroneously rejected. Therefore, we assessed field significance by the false discovery rate (FDR) method following Wilks (2016) to control the FDR. We set $\alpha_{\text{global}} = 0.05$ and $\alpha_{\text{FDR}} = 2\alpha_{\text{global}}$ for spatially autocorrelated fields. The spatial resolution of composite mean fields for statistical tests was reduced to decrease the number of multiple null hypothesis tests: R^* radial and azimuthal grid spacings are 0.1° and ~22.5°, respectively, determined by spatial scales of large differences in the composite mean fields between IN and SS cases. In this study, some tests failed to achieve field significance even though some null hypotheses (i.e., no difference between two groups) were locally (i.e., at grid points) rejected. In this case, the global null hypothesis that all individual gridpoint null hypotheses are true cannot be rejected (Wilks 2016). This is a caveat to interpret the results of this study from the perspective of statistics, although a statistically nonsignificant result does not mean the null hypothesis is true (Amrhein et al. 2019).

3. Statistics of upper-level updrafts

In this section, we characterize upper-level updrafts in the eyewall for both IN and SS cases from two perspectives to confirm the findings of previous studies. One is tied to the magnitudes and azimuthal locations of peak updrafts at upper levels, following Wadler et al. (2018). Another is the WN-1 quasi-stationary, shear-relative envelope structure of vertical motion at upper levels that is manifested in shear environments on the 3–5-h IOP time scale (e.g., Bender 1997; Lonfat et al. 2004; Braun et al. 2006; Braun and Wu 2007; Riemer et al. 2010; Reasor et al. 2013; Rogers et al. 2013).

Figure 1 shows peak updraft magnitudes in the eyewall (R^* = 0.8–1.2) observed within the 11–14-km height range during individual IOPs. Here, the peak updraft is detected from all swaths that comprise a merged analysis (except for two cases with a single swath) during each IOP (Table 1). The magnitude and azimuthal location of the peak updrafts vary greatly among cases. IN cases, however, have peak updrafts concentrated DSL and USL with updraft magnitude greatest USL, consistent with the findings of Wadler et al. (2018). A chi-square goodness of fit test, where the null hypothesis is that the frequencies of peak updrafts in the quadrants are the same, indicates that the concentration of the updrafts DSL and USL is statistically significant at the 95% level. In contrast, SS cases have no statistically significant preference for the azimuthal location of peak updrafts, although 42% of SS cases have peak updrafts concentrated DSL (Table 2). The mean value of the peak updraft magnitudes is 8.9 m s^{-1} for IN cases, whereas 6.5 m s^{-1} for SS cases. This difference is statistically significant at the 95% level with a two-sided Wilcoxon–Mann–Whitney rank-sum test. The feature of vupper-level updrafts that are concentrated DSL and USL is natural because individual convective cells travel cyclonically near the RMW from the downshear-right quadrant (DSR) to USL while developing and weakening (e.g., Reasor et al. 2009). Nevertheless, there is a distinct difference in transient convective activity USL between IN and SS cases.

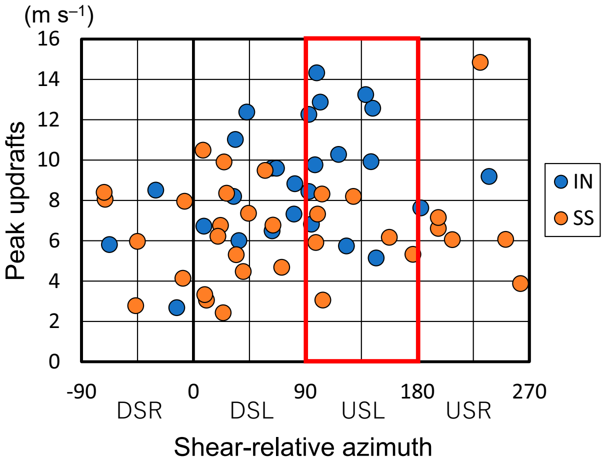

FIG. 1. Scatterplot of peak updraft magnitudes (on the y axis) and their azimuthal locations (on the x axis) observed within $R^* = 0.8$–1.2 and within heights from 11 to 14 km during each intensive observing period (IOP). The red outline indicates the range of USL. The total numbers of IN and SS cases are 27 and 33, respectively.

Next, the locations of maximum WN-1 ascent at upper levels are examined. Here, merged analyses averaged over specified radii are used to obtain the WN-1 component of a quantity, computed by a least squares fitting with the azimuthal data gap allowed up to 90° to obtain as many cases as possible. The amplitude of the WN-1 component, however, can be uncertain when radar coverage is relatively poor and when there are outliers (e.g., very strong updrafts). Therefore, only the azimuthal location of the maximum WN-1 component is examined here. SS cases tend to have very poor radar coverage above 11 km; out of 33 SS cases, there were only 22 SS cases in which WN-1 components above 11-km height were obtained. In contrast, 25 IN cases were obtained in the WN-1 analysis out of 27 cases.

The difference in the locations of maximum WN-1 ascent between IN and SS is distinct at ∼12-km height. Table 2 indicates that 56% of IN cases have maximum WN-1 ascent in the eyewall ($R^* = 0.8$–1.2) USL averaged at 12 ± 0.5-km height, whereas 9% of SS cases do. The preference (i.e., more than 50% of IN cases) for WN-1 ascent USL for IN cases is statistically significant. Although not statistically significant, 45% of SS cases have maximum WN-1 ascent in the upshear-right quadrant (USR), which is inconsistent with the distribution of peak updraft magnitudes (Fig. 1). For some SS cases, the WN-1 w phase appears to be affected by strong downdrafts DSL just inside the RMW rather than strong updrafts USR (not shown). Therefore, a strong quasi-stationary component of the USL ascent at upper levels can be a signal of ongoing intensification.

Some of the SS cases might have concentric eyewalls or outer rainbands, as shown by Rogers et al. (2013). Didlake et al. (2017) showed that the locations of maximum inflow and updrafts in the inner eyewall can azimuthally shift depending on the stages of ERCs. Thus, there is a possibility that WN-1 ascent USR in some SS cases is attributable to the azimuthal shift of peak inflow and updrafts. To assess this possibility, the relationship between the azimuthal locations of WN-1 upper-level ascent and WN-1 low-level (0.5–2.0 km) and midlevel (9 km) radial winds outside the RMW ($R^* = 1.0$–1.5) is examined. Figures 2a and 2b show scatterplots of the phase of WN-1 low-level inflow and midlevel inflow, respectively, versus the phase of upper-level WN-1 vertical motion. Both IN and SS cases have WN-1 low-level inflow peaks concentrated downshear and WN-1 midlevel inflow peaks concentrated USL. This fact does not support the possibility of the azimuthal shift.

In summary, IN cases tend to have maximum quasi-stationary ascent USL at upper levels, whereas SS cases do not have this preference. This difference is consistent with previous studies in that strong ascent USL at upper levels can be a signal of ongoing intensification and observed despite the fact that both IN and SS cases have similar inflow directions at low and middle levels. These findings motivate us to use a composite approach in a shear-relative framework in the next section to compare differences in the asymmetric eyewall structure between IN and SS cases.

4. Composite analysis

To examine the shear-relative asymmetric structure in the eyewall and to permit robust statistical comparisons, we limited our analysis to cases with adequate radar coverage over a deep layer (including 12-km height or higher) and cases with low-level inflow located downshear[1] using the WN-1 analysis results in section 3. Additionally, cases with a remnant eyewall inside the RMW were removed because they make it difficult to examine the kinematic structure inside the eye. Finally, the weakest IN storm was removed so that the composite-mean maximum tangential wind speeds of IN and SS cases at 2-km height become nearly the same (51.4 $\mathrm{m\ s^{-1}}$ for IN cases and 51.7 $\mathrm{m\ s^{-1}}$ for SS cases). Consequently, 18 IN and 15 SS cases were selected for the composite analysis (Table 1). Hereafter, all results shown in this study are based on the selected composite dataset. In the composite analysis, we do not focus on differences in the strength of boundary layer inflow because of the uncertainty in winds retrieved below 1-km height (Fischer et al. 2022) and because strongest inflow is primarily observed below 0.5-km height, which is not resolved here (e.g., Zhang et al. 2011, 2023).

a. Life stages and environmental conditions

Intensity histories of the composite cases (Figs. S1b,c in the online supplemental material) indicate that IN cases are generally much younger than SS cases; 67% of IN cases and 47% of SS cases became tropical-storm strength within 5 days before $t = 0$ h, respectively; the mean duration of tropical storm strength and above is ∼95 h for IN cases and ∼146 h for SS

---

[1] Most cases with storm-relative low-level inflow located upshear have a secondary eyewall or distinct outer rainbands. Another reason for upshear inflow is uncertainty in the calculation of vertical shear (e.g., the area of shear calculation, method of vortex removal, data used, etc.).

TABLE 2. The frequency (%) of peak updraft locations in the eyewall ($R^* = 0.8$–1.2) observed at 11–14 km and maximum WN-1 ascent locations computed from w averaged at 12 ± 0.5-km height in the eyewall ($R^* = 0.8$–1.2) for IN and SS cases based on the shear-relative quadrant. Boldface with italic denotes a statistically significant difference in the frequency of peak updraft locations and maximum WN-1 ascent locations between quadrants at the 95% level with a chi-square goodness of fit test. In this test, the null hypothesis is that the frequencies of peak updraft locations maximum WN-1 ascent locations in the four quadrants are the same. DSR, DSL, USL, and USR denote the downshear-right, downshear-left, upshear-left, and upshear-right quadrants, respectively.

	No. of samples	DSR	DSL	USL	USR	p value
Peak updraft (IN)	*27*	***11***	***37***	***44***	***7***	***0.011***
Peak updraft (SS)	33	18	42	21	18	0.143
Max WN-1 ascent (IN)	*25*	***16***	***16***	***56***	***12***	***0.005***
Max WN-1 ascent (SS)	22	27	18	9	45	0.095

cases. In addition, only 22% of IN cases had reached 100 kt and above and then weakened before $t = 0$ h due to an eyewall replacement cycle, dry air intrusion, strong vertical shear, or a combination of them, according to TC reports (Stewart 2004; Cangialosi et al. 2018; Beven and Wroe 2019; Zelinsky 2019), whereas 80% of SS cases had done so. IN cases for the composite are TCs in the middle of intensification.

SHIPS environmental conditions of the composite cases (Table 3) indicate no statistically significant difference at the 95% level between IN and SS cases, except for 150 and 200-hPa temperatures (T150 and T200). SS cases, however, are located in slightly more unfavorable environments than IN cases. For example, 11% of IN cases are over waters with ocean heat content (OHC) ≤ 30 kJ cm^{-2}, whereas 33% of SS cases are. Furthermore, 17% of IN cases are affected by deep-layer shear (SHDC) ≥ 8 m s^{-1}, whereas 47% of SS cases are. Of IN cases, 22% have potential intensification [POT ≡ maximum potential intensity (MPI) − Vm] ≤ 30 kt, whereas 40% of SS cases do. Only 6% of IN cases are in environments with relative humidity at 700–500 hPa (RHMD) ≤ 50%, whereas 33% of SS cases are. The significantly lower T150 and T200 for IN cases than SS cases are likely responsible for the slightly higher MPI and thus POT since there is no difference in sea surface temperature (SST) between IN and SS cases. The inherent differences in the life stages and the environment between IN and SS cases are likely an important contributor to their difference in intensification rate, since more mature storms, which tend to be SS, have accumulated angular momentum in their outer cores, developed rainbands, and potentially secondary eyewalls (Sitkowski et al. 2011; Musgrave et al. 2012; Rozoff et al. 2012; Rogers et al. 2013).

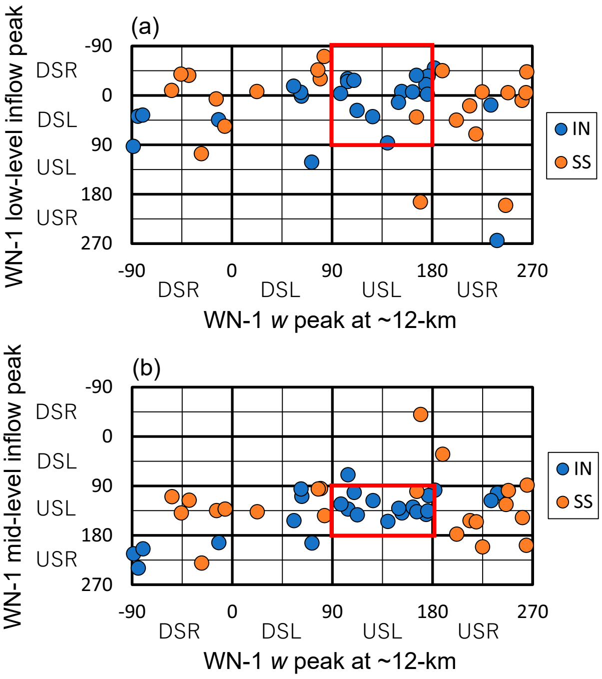

FIG. 2. (a) Scatterplot of the azimuthal location of maximum WN-1 low-level mean (at heights of 0.5–2.0 km) inflow outside the RMW ($R^* = 1.0$–1.5) on the y axis and the azimuthal location of maximum WN-1 vertical motion in the eyewall ($R^* = 0.8$–1.2) averaged at 12 ± 0.5-km height on the x axis. (b) As in (a), but for the azimuthal location of maximum WN-1 midlevel (at 9-km height) inflow outside the RMW ($R^* = 1.0$–1.5) on the y axis. Not all cases are plotted due to the limitation of maximum radar echo height; the total numbers of IN and SS cases plotted are 25 and 22, respectively. The red box denotes the quadrants where IN cases are concentrated.

b. Axisymmetric vortex structure

Here, we briefly show differences in the composite-mean axisymmetric structure between IN and SS cases in the expanded composite datasets (Fig. 3). Near the RMW ($0.5 < R^* < 1.5$), there is little difference in tangential wind $\overline{v}$ (an overbar denotes the azimuthal mean) between IN and SS cases as a result of the composite sample selection (Figs. 3a,b). The maximum tangential wind is seen below 1-km height. The mean RMW of IN cases (27.3 km) is slightly smaller than that of SS cases (32.8 km). IN cases have weak inflow below 4-km height just outside the RMW (Fig. 3b), whereas SS cases generally have outflow there except in the boundary layer (Fig. 3e). The difference in radial wind $\overline{u}$ is locally significant in the vicinity of the RMW at 2-km height (Fig. 3c). As for vertical velocity $\overline{w}$, IN cases have slightly stronger ascent inside $R^* = {\sim}1.0$ than SS cases (Fig. 3f).

In the outer region beyond $R^* = 2.0$ (corresponding to ~50–120-km radii), IN cases have radii of 25, 30, and 35 m s^{-1} located much more inward (Fig. 3a) compared to those of SS cases (Fig. 3d). The SS composite has outflow and inflow inside and outside $R^* = {\sim}2.5$, respectively, just above 2-km height. Secondary eyewall formation (SEF) has been shown to be accompanied by a radial expansion of the tangential wind field (e.g., Bell et al. 2012; Wu et al. 2012; Huang et al. 2012; Rozoff et al. 2012).

TABLE 3. Storm location (LON: longitude and LAT: latitude), best track intensity (Vm; kt), intensity change (ΔVm; kt (12 h)$^{-1}$, and SHIPS environmental conditions. Abbreviations: sea surface temperature (SST; °C), ocean heat content (OHC; kJ cm^{-2}), 850–200-hPa shear (SHDC; m s^{-1}), 850–500-hPa shear (SHRS; m s^{-1}), maximum potential intensity (MPI; kt) from Bister and Emanuel (2002), potential intensification (POT; MPI − Vm), 150-hPa temperature (T150; °C), 200-hPa temperature (T200; °C), 250-hPa temperature (T250; °C), 850–700-hPa relative humidity (RHLO; %), 700–500-hPa relative humidity (RHMD; %), and 500–300-hPa relative humidity (RHHI; %). Boldface p values denote statistically significant differences at the 95% level with a two-sided Wilcoxon–Mann–Whitney rank-sum test. Values of LON, LAT, and Vm are at $t = 0$ h, a value of ΔVm is an intensity change from $t = -6$ to +6 h, and values of environmental conditions are 12-h mean values from $t = -12$ to 0 h. The reason for the difference in the averaging period between ΔVm and environmental conditions is to consider a time lag during which environmental conditions affect intensity. The total numbers of IN and SS cases are 18 and 15, respectively.

	LON	LAT	Vm	ΔVm	SST	OHC	SHDC	SHRS	MPI	POT	T150	T200	T250	RHLO	RHMD	RHHI
IN (mean)	82.9	20.8	110.3	21.4	29.0	54.4	5.6	3.0	147.3	46.6	−67.1	−52.5	−40.3	70.7	61.1	53.5
IN (std dev)	23.8	5.8	14.1	8.9	0.6	20.7	2.2	1.5	6.7	20.0	0.7	0.8	0.9	6.1	8.0	7.4
SS (mean)	78.9	22.3	108.3	0.3	29.0	50.2	7.1	3.0	142.2	33.7	−65.8	−51.6	−39.8	67.9	57.5	53.3
SS (std dev)	24.4	6.0	13.5	4.0	0.6	24.1	2.7	1.0	8.7	17.9	1.3	1.0	1.0	7.7	12.1	11.4
p value	0.515	0.303	0.489	**0.000**	0.870	0.426	0.068	0.971	0.073	0.065	**0.002**	**0.018**	0.082	0.375	0.600	0.885

In fact, 6 SS cases have a weak secondary peak of tangential wind in the outer region (not shown).

c. *Asymmetric eyewall structure*

In this subsection, we examine differences in the asymmetric convective eyewall structure between IN and SS cases in a shear-relative framework. In particular, we focus on the relationship between downshear convection and USL upper-level ascent. Hereafter, we use analyses based on individual radial passes (swath data) to investigate transient convective-scale features unless otherwise noted.

Figure 4 shows the composite-mean eyewall structure just inside the RMW ($R^* = 0.8$–1.0), where the most significant differences are seen at 12-km height (Fig. S2), for IN and SS cases. In general, there is ascent downshear and descent upshear below ~10-km height, and the strongest reflectivity is left of shear (Figs. 4a,b), consistent with Black et al. (2002) and DeHart et al. (2014). IN cases have significantly stronger ascent USL above 8-km height, whereas SS cases have slightly stronger descent inside the downshear eyewall above 11-km height. Significantly stronger ascent is also seen at low levels azimuthally upwind of the USL ascent for IN cases (i.e., downshear below 5-km height, Fig. 4c). Furthermore, there is significantly stronger ascent DSR at $R^* = \sim 0.5$ at 2-km height for IN cases (Fig. S3). The DSR quadrant is a region where convection initiates (Black et al. 2002; DeHart et al. 2014). The local minimum of ascent near the interface of the DSL and USL quadrants at ~9-km height for IN cases (Fig. 4a) is due to the fact that the eyewall slopes more outward with height DSL than USL because of the vortex tilt downshear (Fig. S4).[2] IN cases have higher reflectivity below the USL ascent (Fig. 4d) and stronger descent USR downwind and below the higher reflectivity (Fig. 4c). Therefore, the eyewall composite suggests that the feature of strong ascent USL for IN cases can be traced back to features of strong ascent upwind (i.e., DSL and DSR) as an evolution of convective development. This helical nature of updrafts in the eyewall has been illustrated by Heymsfield et al. (2001) and Black et al. (2002).

To look at the secondary circulation associated with the strong ascent from downshear to USL, the quadrant-average cross sections of shear-relative composite w, radial velocity, and tangential velocity for IN cases are shown in Figs. 5a–d. Low-level inflow that penetrates the eyewall is seen DSR inside the RMW below 4-km height, where a negative radial gradient of radial velocity suggests convergence and the beginning of the low-level ascent (Fig. 5b). In the DSL quadrant, low-level outflow inside the RMW below 3-km height converges with low-level inflow outside the RMW, in association with the strong, deep ascent from the boundary layer to heights above 14 km (Fig. 5a). In the USL quadrant, strong ascent exists above 8-km height, and weak descent is seen near the RMW below 8-km height (Fig. 5c), which is similar to a conceptual model of old convection, a convective

---

[2] As for vortex tilt, there is no difference between IN and SS cases, and vortices tend to tilt downshear (Fig. S4). The features of vortex tilt are the same as those of Rogers et al. (2013).

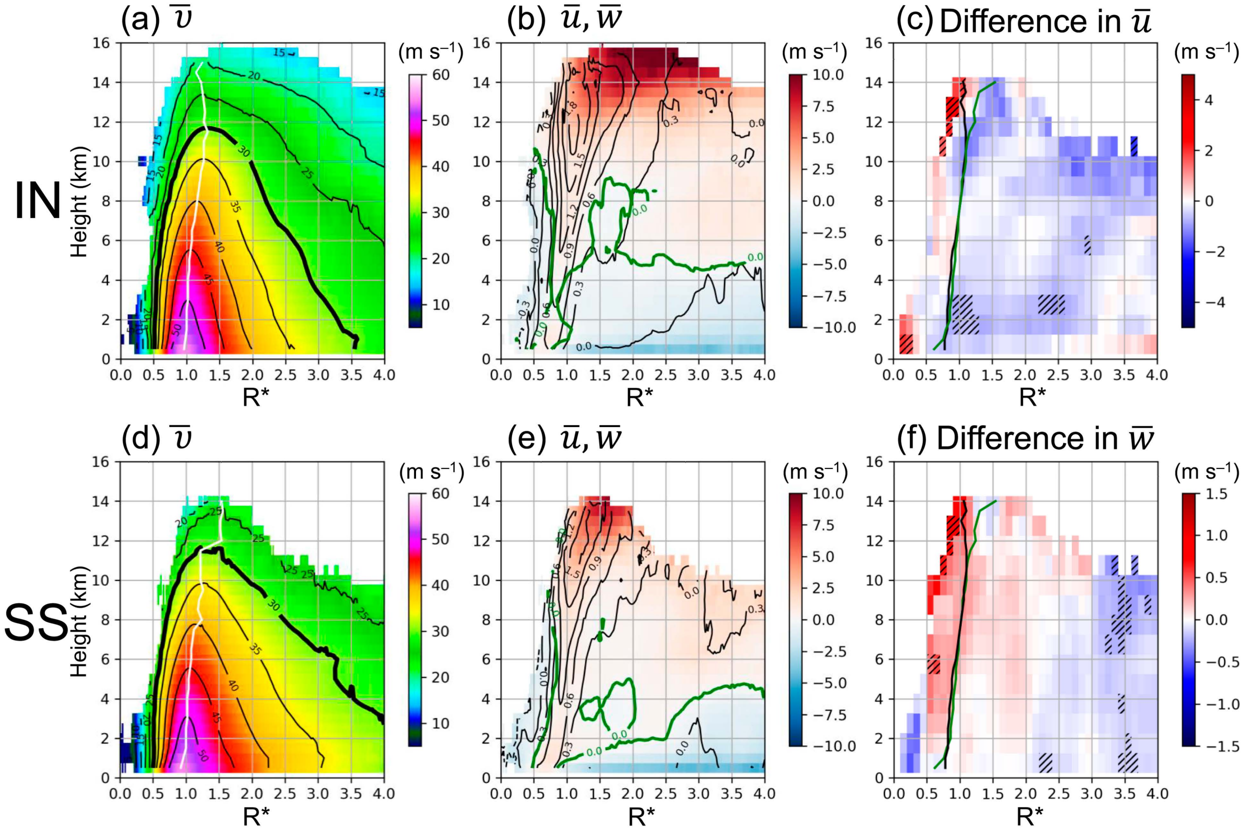

FIG. 3. Radius–height plots of composite-mean axisymmetric (a) tangential wind $\overline{v}$ (both colors and contours;, m s^{-1}), (b) radial wind $\overline{u}$ (colors; m s^{-1}) and vertical velocity $\overline{w}$ (black contours; m s^{-1}) fields for IN cases, and (c) differences in the composite-mean $\overline{u}$ between IN and SS cases (IN minus SS; colors; m s^{-1}). (d)–(f) As in (a)–(c), but for SS cases in (d) and (e) and for differences in the composite-mean $\overline{w}$ in (f). Hatched areas are statistically significant at the 95% significance level using a two-sided Wilcoxon–Mann–Whitney rank-sum test. The white line and thick black line in (a) and (d) denote the RMW and the isoline of 30 m s^{-1}, respectively; the green line in (b) and (e) denotes a radial wind speed of 0.0 m s^{-1}; the black line in (c) and (f) denotes the radius of maximum ascent for IN cases; and the green line in (c) and (f) denotes the radius of maximum ascent for SS cases. A minimum of eight missions at any given location in radius–height space is required to make the composite field. The radius is normalized by the RMW at 2-km height (i.e., $R^* = r$/RMW).

system that is mature and transitioning to primarily stratiform precipitation (e.g., Houze 1997). The midlevel inflow layer sandwiched between the low-level and upper-level outflow layers is evident. The midlevel inflow may be attributed to a combination of environmental wind shear, vortex tilt relative to the low-level center, and inflow induced by strong upper-level ascent and stratiform precipitation processes (e.g., Didlake and Houze 2013). The tangential wind speed (~40 m s^{-1}) is much faster than the inflow speed (~5 m s^{-1}), suggesting that inflowing air mostly comes from DSL near the eyewall, not from the drier environment.

SS cases (Figs. 5e–h) have an asymmetric structure similar to IN cases, but three noteworthy differences exist. Figure 6 shows the quadrant difference fields between IN and SS cases. The first noteworthy difference is radial wind below 7-km height downshear: IN cases have slightly stronger inflow at ~2-km height and stronger outflow inside the RMW and above the low-level inflow layer in the vicinity of the RMW within $R^* = 1.5$ (Figs. 6a,b). These radial wind differences are associated with the stronger ascent below 8-km height for IN cases, indicative of a stronger local secondary circulation in the downshear eyewall. The second noteworthy difference is the radial location of ascent. Positive and negative differences in w between IN and SS cases are distributed vertically (i.e., red and blue sloped stripes) near $R^* = 1$ on the upshear side (Figs. 6c,d), indicating that the ascent area of IN cases is located inward relative to that of SS cases. The third noteworthy difference is a mid- to upper-level transverse circulation USL (Fig. 6c). For IN cases, there is midlevel convergence in the eyewall region associated with inflow at 5–11-km height and upper-level divergence associated with outflow above 12-km height (Fig. 7a), suggesting that the diabatically induced secondary circulation is enhanced above 5-km height. In contrast, SS cases have no convergence in the eyewall region associated with inflow at 5–7-km height (Fig. 7b), resulting in a weak secondary circulation above 5-km height.

To confirm the circumstantial evidence of convective development from DSR to USL, Fig. 8 shows the CFADs of w in DSR, DSL, and USL for IN cases and their differences between

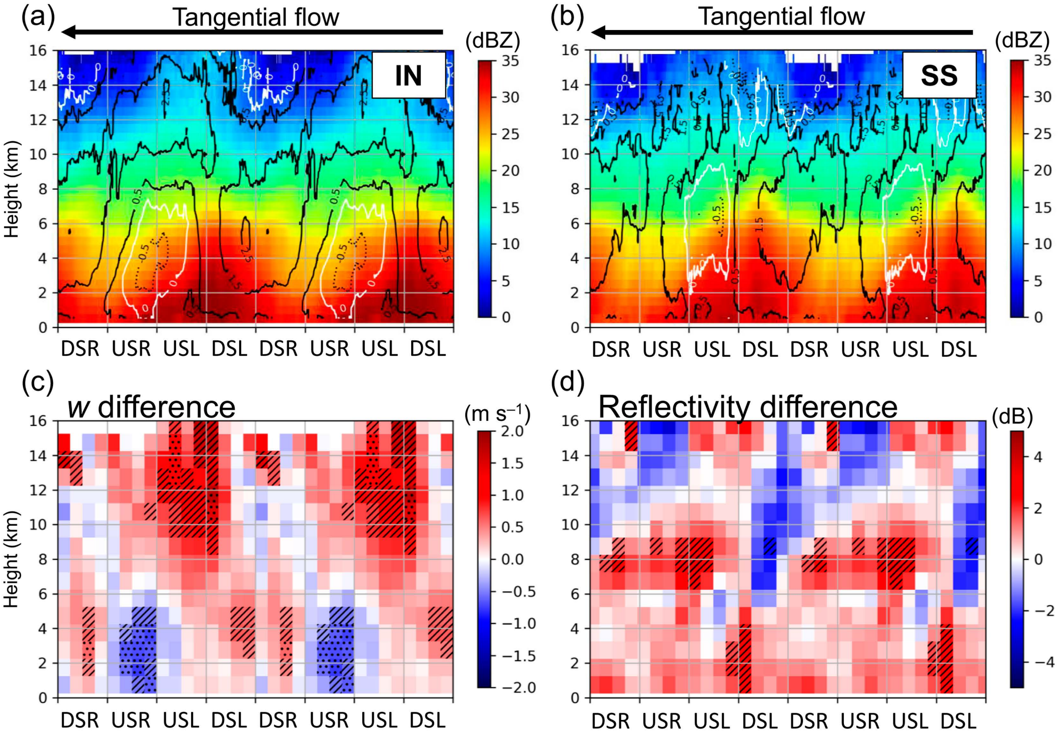

FIG. 4. Azimuth–height plots of composite-mean reflectivity (colors; dBZ) and w (contours; m s^{-1}) averaged over the eyewall region ($R^* = 0.8$–1.0) for (a) IN and (b) SS cases, and differences in (c) w (m s^{-1}) and (d) reflectivity (dBZ) in the eyewall region between IN and SS cases (IN minus SS). Hatching indicates areas that are significant at the 95% significance level with a two-sided Wilcoxon–Mann–Whitney rank-sum test, and stippling indicates areas where p values pass an FDR test for field significance ($\alpha_{\mathrm{global}} = 0.05$). Values of w are contoured at −1.0, −0.5, 0, 0.5, and 1.5 m s^{-1} and 2.5 m s^{-1}. Negative and zero values are denoted by dashed and white contours, respectively. The plots are extended to two revolutions. "DSR," "DSL," "USL," and "USR" denote downshear right, downshear left, upshear left, and upshear right, respectively. A minimum of 11 radial passes at any given location in azimuth–height space is required to make the composite field.

IN and SS cases. The radial domain of each CFAD was selected to target regions containing statistically significant differences in w (Fig. 6; Figs. S2 and S3). The CFADs have been employed to investigate a life cycle of convection through differences in ensemble properties of the whole sample of convective cells (Yuter and Houze 1995; Hence and Houze 2011; DeHart et al. 2014). The w CFADs of IN cases show that in DSR, the frequency of ascent is higher than that of descent below 10-km height, implying convective initiation. In DSL, ascent is more frequent than descent at all heights, which shows characteristics of deep convection. In USL, ascent is more frequent above 10-km height, and descent is more frequent at 3–7-km heights, consistent with the pattern of more mature convection and stratiform precipitation (e.g., Houze 1997). Furthermore, compared to SS cases, IN cases have higher frequencies of 2–4 m s^{-1} updrafts at 1–7-km heights in DSR, 2–6 m s^{-1} updrafts at 6–15-km heights in DSL, and 2–8 m s^{-1} updrafts at 9–16-km heights and weak downdrafts below 5-km height in USL. Consistent with the downwind advection of convective cells by the hurricane-strength tangential winds (Fig. 3a), the altitude of the peak difference in the frequency of moderate updrafts (2–6 m s^{-1}) increases from DSR to USL. Meanwhile, SS cases are characterized by a higher frequency of downdrafts, including strong downdrafts (<-4 m s^{-1}), at upper levels DSL and USL. Therefore, the CFADs of w suggest that IN cases have stronger convective cells than SS cases and that these convective cells initiate DSR well inside the RMW ($R^* = 0.5$–0.8) and develop as they rotate to the USL quadrant where they transition into stratiform systems.

d. Low-level kinematic field

In this subsection, we characterize the low-level kinematic field (at 2-km height) associated with the downshear eyewall convection. Figure 9a shows the asymmetric components of composite-mean vorticity and wind fields at 2-km height for IN cases by subtracting the azimuthal mean at each radius. Inside the RMW, IN cases have a positive vorticity anomaly DSL, which is a statistically significant difference from SS cases (Fig. 9c).[3] Along with vorticity anomalies, IN cases have

---

[3] Note that IN cases tend to have slightly greater azimuthal-mean relative vorticity than SS cases because of the smaller RMW. Assume a Rankine vortex. Using the mean RMW (Rmw) and the maximum tangential wind speed (Vmax) at 2-km height, the relative vorticity inside the RMW (= 2 × Vmax/Rmw) is calculated as 3.77×10^{-3} s^{-1} for IN cases and 3.15×10^{-3} s^{-1} for SS cases.

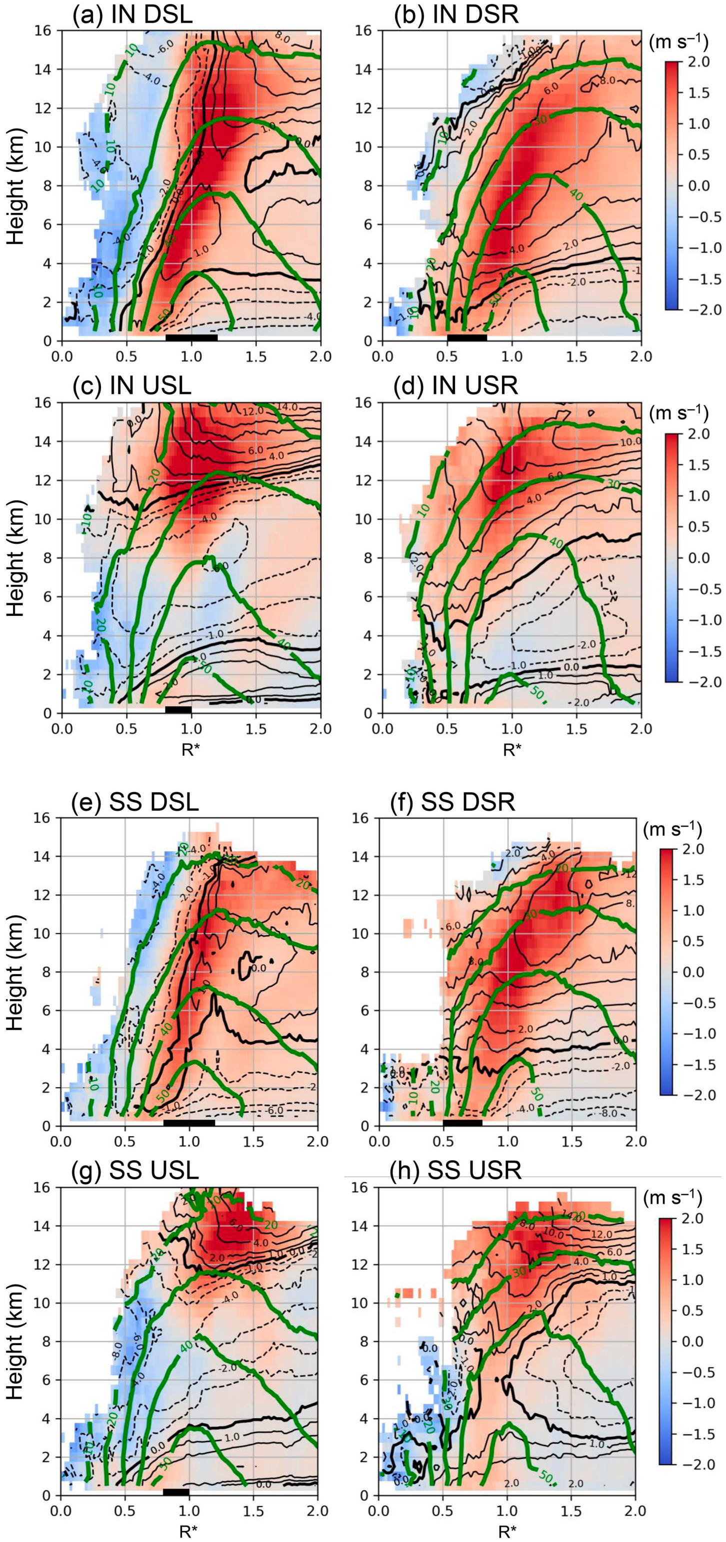

FIG. 5. (a)–(d) Quadrant-average cross sections of shear-relative composite *w* (shading; m s^{-1}), radial velocity (black contours; m s^{-1}), and tangential velocity (green contours; m s^{-1}) for IN cases. Values of radial velocity are contoured at 0, ±1, and ±2 m s^{-1} and from ±2 m s^{-1} at an interval of 2 m s^{-1}. Values of tangential velocity are contoured at an interval of 5 m s^{-1}. Negative values are

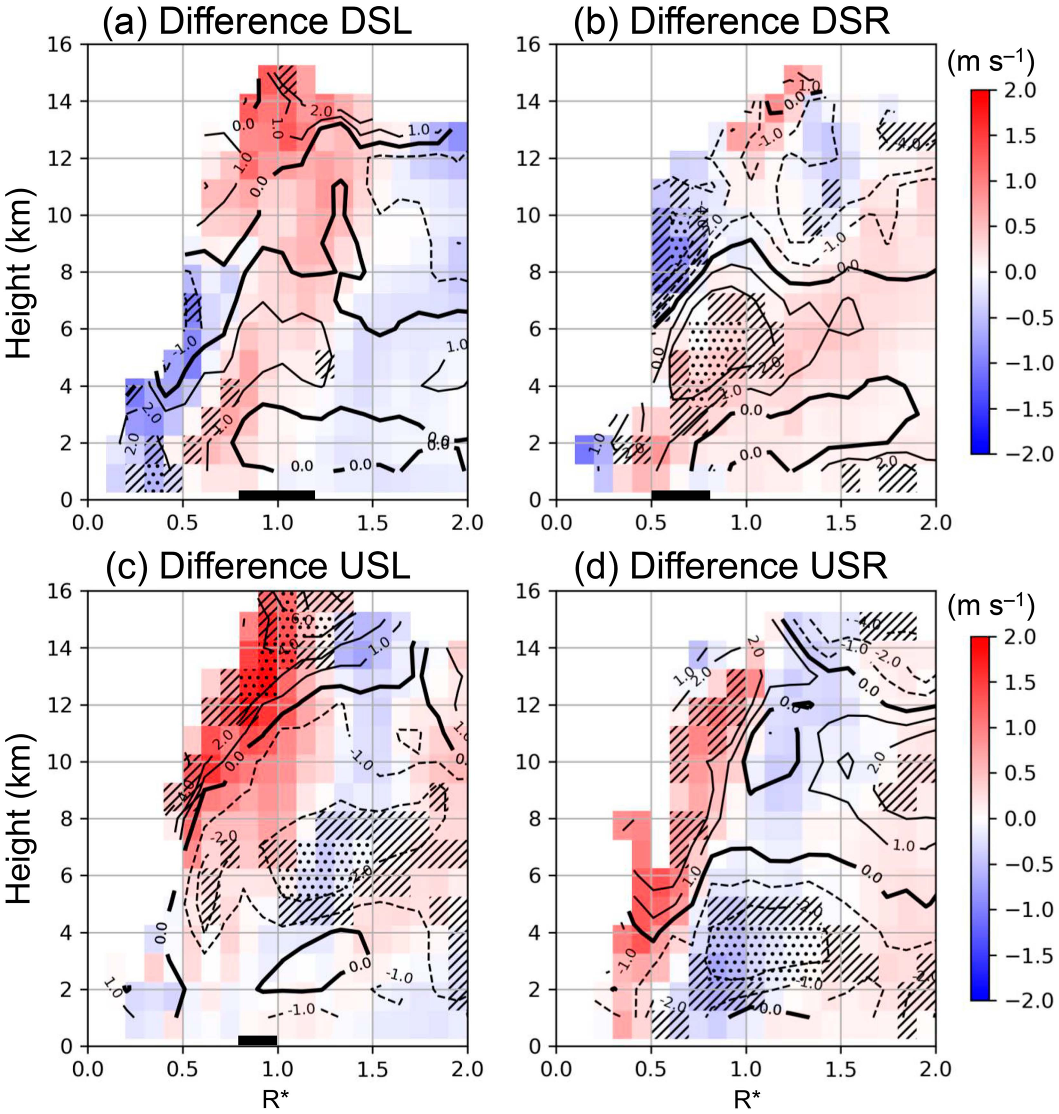

FIG. 6. As in Figs. 5a–d, but for difference fields between IN and SS cases (IN minus SS). Differences in w and radial velocity are shown in colors (m s^{-1}) and black contours (at 0, ±1, and ±2 m s^{-1} and from ±2 m s^{-1} at an interval of 2 m s^{-1}), respectively. Negative values are denoted by dashed contours. Hatching indicates areas of differences in radial velocity that are significant at the 95% significance level with a two-sided Wilcoxon–Mann–Whitney rank-sum test, and stippling indicates areas where p values pass an FDR test for field significance ($\alpha_{\text{global}} = 0.05$). Differences in the tangential wind are not shown. The radial domain for each CFAD of Fig. 8 is indicated by the black line at the bottom of the panels. Statistical test results for difference in radial velocity are given in Fig. S5.

inflow in the right-of-shear region inside the RMW and outflow downshear in the eye that collides with inflow outside the RMW. Note that the asymmetric component of the composite does not represent the instantaneous asymmetric structure of a TC. As shown by Braun et al. (2006) and Reasor et al. (2009), there are likely smaller-scale mesovortices that rotate around the eyewall cyclonically with vorticity increasing downshear and decreasing upshear and, as a result, a WN-1 pattern emerges in the composite field. Meanwhile, SS cases have an asymmetric flow pattern in the eye that does not collide with

---

←

denoted by dashed contours. The radius is normalized by the RMW at 2-km height. A minimum of 11 radial passes at any given location in radius–height space is required to make the composite field. The radial domain for each CFAD of Fig. 8 is indicated by the black line at the bottom of the panels. (e)–(h) As in (a)–(d), but for SS cases.

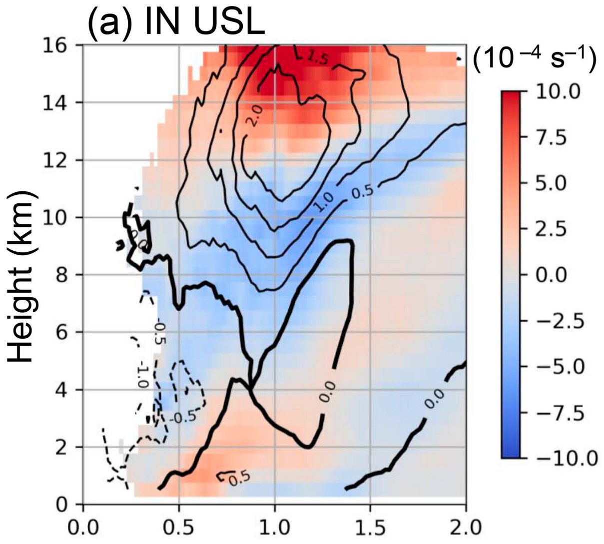

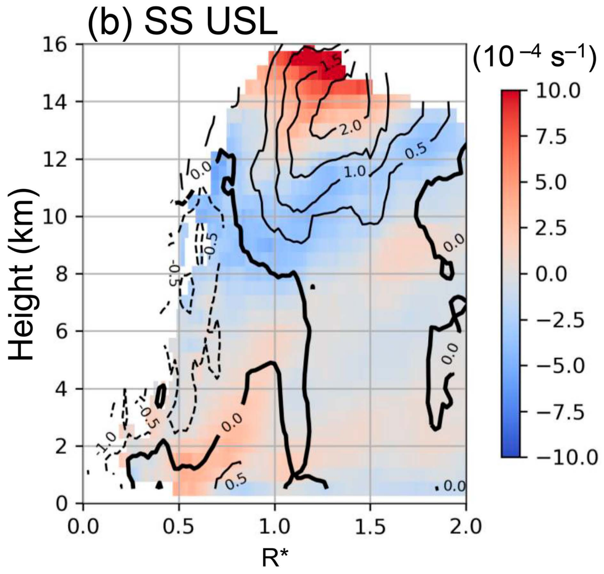

FIG. 7. USL-average cross sections of shear-relative composite divergence (shading; 10^{-4} s^{-1}) and w (black contours; m s^{-1}) for (a) IN and (b) SS cases. Values of w are contoured at an interval of 0.5 m s^{-1}. Negative and zero values are denoted by dashed and thick contours, respectively. The radius is normalized by the RMW at 2-km height. A minimum of 11 radial passes at any given location in radius–height space is required to make the composite field.

inflow outside the RMW on the downshear side (Fig. 9b). The differences in radial wind downshear and USR inside the RMW between IN and SS cases are locally significant (Fig. 9d).

Because vorticity has a large spatial variance that can affect an asymmetric pattern of the composite-mean vorticity field (not shown), WN-1 vorticity patterns for individual cases are also examined. The histogram of the patterns inside the RMW (R^* = 0.6–0.9) at 2-km height (Fig. 9e) indicates that 44% and 28% of IN cases have maximum WN-1 vorticity DSL and USL, respectively, whereas SS cases appear to have no such preference. The configuration of maximum WN-1 vorticity located DSL or USL inside the RMW allows for outflow in the eye on the downshear side. The positive vorticity anomaly USR in the SS composite (Fig. 9b) is likely an artifact of the composite because only three cases contribute to the positive anomaly USR (Fig. 9e), and one of them has a large positive anomaly there (not shown). That being said, the low-level inflow in the eye downshear and low-level outflow USR in the SS composite are significant features because of the sufficient sample size for the composite analysis (Fig. 9d).

Figure 10 shows composited divergence fields of IN and SS cases at 2-km height. For IN cases, low-level convergence is significantly enhanced downshear inside the RMW (R^* = 0.7–0.9), where low-level outflow meets with low-level inflow associated with the vertical shear. Such convergence would tend to increase vorticity through vortex stretching, consistent with the positive vorticity anomaly DSL. For SS cases, the convergence zone inside the RMW at 2-km height is limited, in particular, in the convective initiation region DSR (Fig. 8).

e. Relation to hurricane intensity change

We have shown that IN cases have more vigorous eyewall convection, which particularly manifests in the USL upper-level region, than SS cases. In this subsection, we examine how differences in eyewall convection are related to differences in vertical mass flux in the eyewall region and tangential wind tendency from the perspective of vortex evolution.

Figure 11a shows the vertical profile of ascent, descent, and net (the sum of ascent and descent) mass flux in the eyewall region (R^* = 0.75–1.25) for IN and SS TCs, normalized by the maximum ascent mass flux value (i.e., the value at 4-km height). For IN cases, the net vertical mass flux increases with height up to ~5 km and then is almost constant up to 10 km. In contrast, the net vertical mass flux of SS cases decreases above 4 km. The difference in the net mass flux profile below 10-km height between IN and SS cases is mostly associated with the difference in descent mass flux: greater contribution of descent mass flux below 6-km height and smaller contribution of descent mass flux above 6-km height for IN cases than for SS cases. Above 10-km height, IN cases are characterized by greater ascent mass flux than SS cases. The difference in upper-level mass flux to distinguish between IN and SS cases is consistent with the result of Hazelton et al. (2017b) in that the largest differences in upward mass flux between IN and weakening storms appear above 9-km height.

Figures 11b and 11c show the azimuth–height plot of net vertical mass flux normalized by the maximum net mass flux value. The differences in mass flux between IN and SS cases described above mainly appear upshear. For IN cases, the net downward mass flux is larger upshear below 6-km height, and the net upward mass flux is larger USL above 8-km height, compared with SS cases. These differences are also seen in the w CFAD of USL (Fig. 8f) although the radial region of the w CFAD is limited inside the RMW. The old convection and stratiform precipitation accompanied by low-level descent and upper-level strong ascent upshear for IN cases

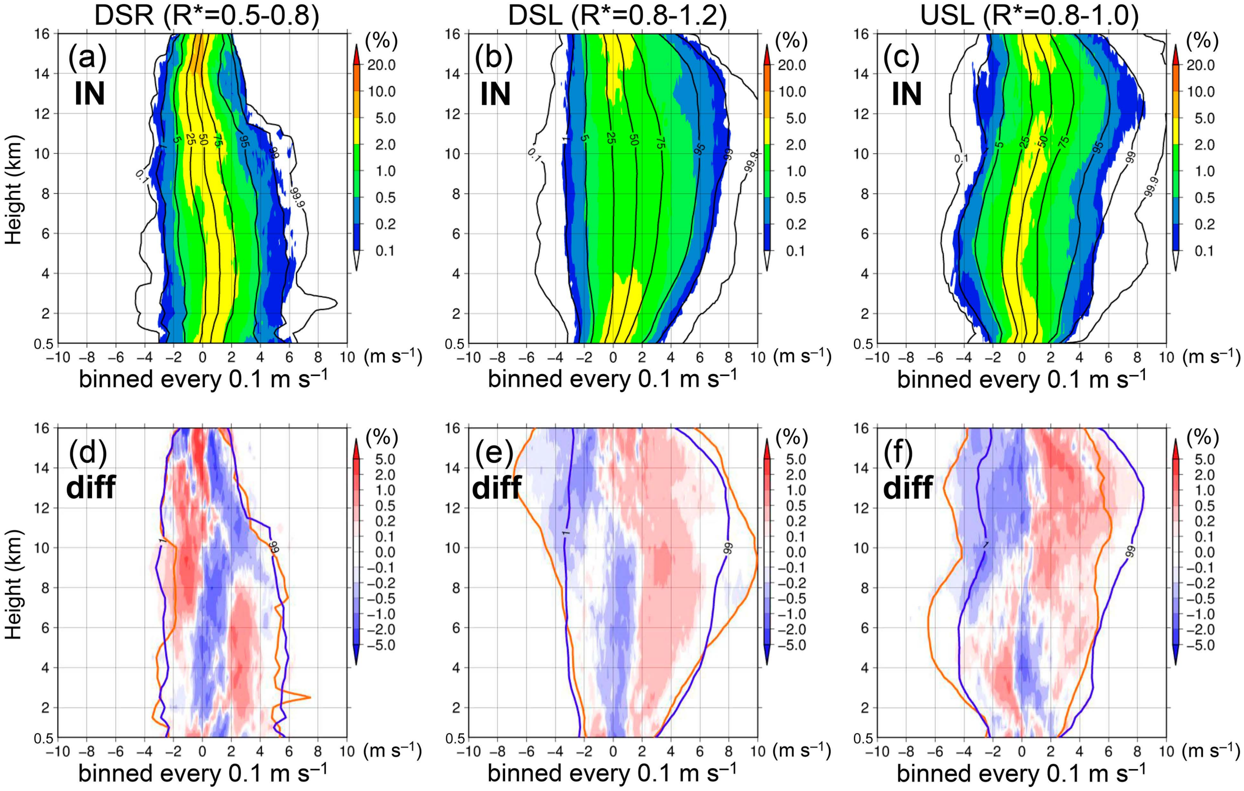

FIG. 8. Contoured frequency by altitude diagram (CFAD) of w in (a) DSR of $R^* = 0.5$–0.8, (b) DSL of $R^* = 0.8$–1.2, and (c) USL of $R^* = 0.8$–1.0 for IN cases. (d)–(f) As in (a)–(c), but for differences in CFAD between IN and SS cases (IN minus SS). Contours in (a)–(c) denote percentiles (0.1st, 1st, 5th, 25th, 50th, 75th, 95th, 99th, and 99.9th percentiles) of the cumulative distributions of w. The blue (orange) contours in (d)–(f) denote 1st and 99th percentiles of the cumulative distributions of w for IN (SS) cases. The radial domain of each CFAD is indicated by the black line at the bottom of each quadrant panel of Figs. 5 and 6. The data are obtained from swath data files for each group.

contribute to the vertical profile of the net mass flux in the eyewall region.

Although it is unlikely that the USL upper-level ascent drives the low-level vortex spinup, strong USL ascent may contribute to the development of a vortex at mid and upper levels. The temporal evolution of axisymmetric tangential wind $\overline{v}$ at a given radius in the free atmosphere can be approximately evaluated by the azimuthal mean of $-u\zeta_a$ and $-w(\partial v/\partial z)$:

$$\frac{\partial \overline{v}}{\partial t} = -\overline{u\zeta_a} - \overline{w\frac{\partial v}{\partial z}}, \tag{1}$$

where z is the physical height and $\zeta_a = f + \zeta$ is the vertical component of absolute vorticity. Here, f is the Coriolis parameter and $\zeta = (\partial v/\partial r) + (v/r) - r^{-1}(\partial u/\partial \lambda)$ is the vertical component of relative vorticity. The first term on the right-hand side of (1) is the radial flux of absolute vorticity, and the second term is the vertical advection of tangential momentum. As with Reasor et al. (2009), we did not compute the sum of the two terms as a diagnosed tendency that is usually a small residual of large positive and negative terms. This is because, strictly speaking, TDR observations do not present a snapshot kinematic field with rich radar coverage, and thus the residual of terms is not meaningful for evaluating a tendency even qualitatively. Therefore, we focus on differences in the shear-relative structure of the individual contributions to the tangential momentum tendency.

Figure 12 shows azimuth–height plots of $-u\zeta_a$ and $-w(\partial v/\partial z)$ averaged over the eyewall region and their differences between IN and SS cases. The positive areas of $-u\zeta_a$ are more predominant than the negative areas in the lower free atmosphere ($z = 1$–3 km) of IN cases (Fig. 12a), whereas the positive areas are limited there for SS cases (Fig. 12b). At heights of 4–10 km, positive and negative values due to downshear outflow and upshear inflow, respectively, are more evident in IN cases due to the stronger secondary circulation (Fig. 6) than in SS cases (Fig. 12e). Above 10-km height, the positive contributor to $\partial\overline{v}/\partial t$ is $-w(\partial v/\partial z)$. A distinct difference in $-w(\partial v/\partial z)$ between IN and SS cases is seen USL above 10-km height (Fig. 12f). Because there is little difference in $\partial v/\partial z$ between IN and SS cases (not shown), the distinct difference is primarily caused by the difference in the magnitude of ascent. Compared to SS cases, the larger local positive value of $-w(\partial v/\partial z)$ of IN cases contributes to larger positive $-\overline{w(\partial v/\partial z)}$. In fact, the mean value of $-\overline{w(\partial v/\partial z)}$ at 12-km height of IN cases is 5.1×10^{-3} m s^{-2}, whereas that

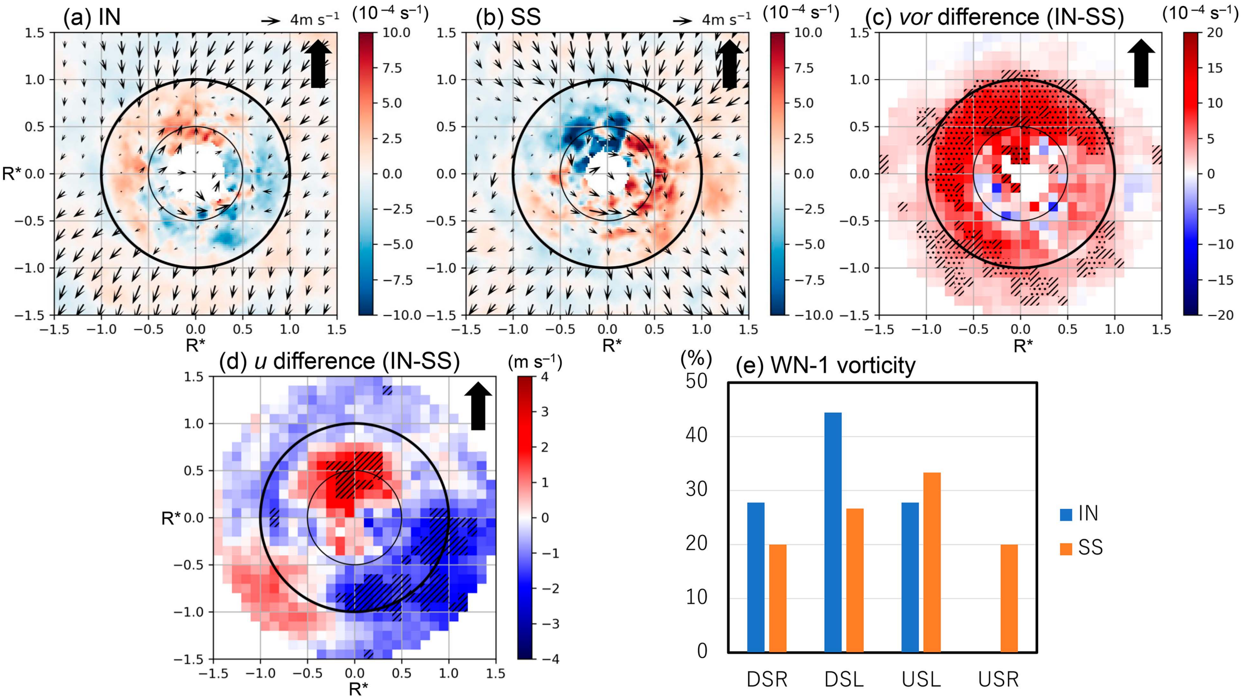

FIG. 9. Asymmetric component of the composite-mean relative vorticity field (colors; 10^{-4} s^{-1}) and composite-mean wind field (vectors) at 2-km height for (a) IN and (b) SS cases. Difference in (c) relative vorticity (10^{-4} s^{-1}) and (d) radial velocity (m s^{-1}) at 2-km height within $R^* = 1.5$ between IN and SS cases (IN minus SS). Hatching indicates areas that are significant at the 95% significance level using a two-sided Wilcoxon–Mann–Whitney rank-sum test, and stippling indicates areas where p values pass an FDR test for field significance ($\alpha_{\mathrm{global}} = 0.05$). The fields of (a)–(d) are plotted on a shear-relative framework, and the vertical shear vector is drawn in the top-right corner of each panel. The $R^* = 0.5$ and 1 are denoted by the thin and thick circles, respectively. A minimum of 11 radial passes at any given location is required to make the composite field. (e) Frequency of the azimuthal locations of maximum WN-1 vorticity at 2-km height based on shear-relative quadrants in the region of $R^* = 0.6$–0.9 for IN and SS cases. The method for obtaining the WN-1 vorticity is the same as those in Fig. 2.

of SS cases is 3.9×10^{-3} m s^{-2}. Therefore, strong USL ascent for IN cases contributes to an increase in $-\overline{w(\partial v/\partial z)}$ in the sense of vortex spinup (i.e., an increase in $\partial\overline{v}/\partial t$) at mid and upper levels (z = 8–14 km). Although the actual total tendency cannot be diagnosed due to the limitation of the dataset, the results suggest that IN cases have greater potential for their vertical development with the aid of strong USL upper-level ascent than SS cases.

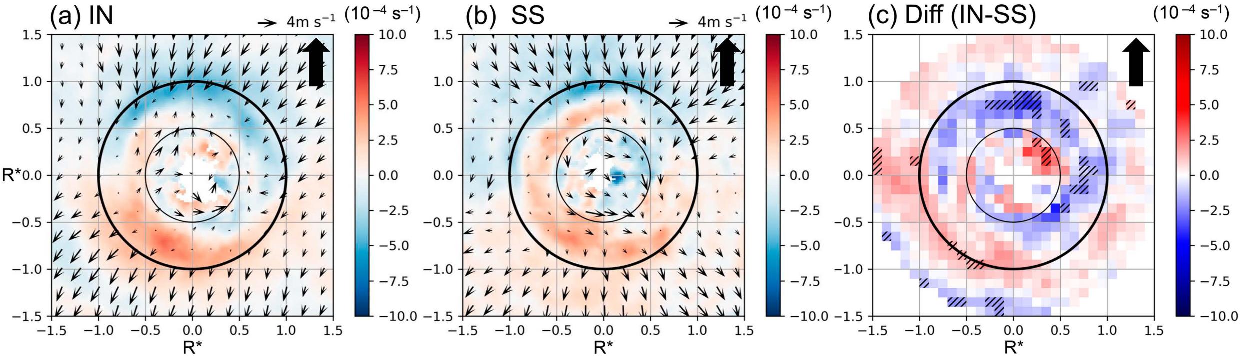

FIG. 10. Composite-mean divergence (10^{-4} s^{-1}) at 2-km height for (a) IN cases, (b) SS cases, and (c) the difference in divergence within $R^* = 1.5$ between IN and SS cases (IN minus SS). Vectors denote the asymmetric component of the composite-mean wind field at 2-km height. Hatched areas are statistically significant at the 95% significance level with a two-sided Wilcoxon–Mann–Whitney rank-sum test. The fields are plotted on a shear-relative framework, and the vertical shear vector is drawn in the top-right corner of each panel. The $R^* = 0.5$ and 1 are denoted by the thin and thick circles, respectively. A minimum of 11 radial passes at any given location is required to make the composite field.

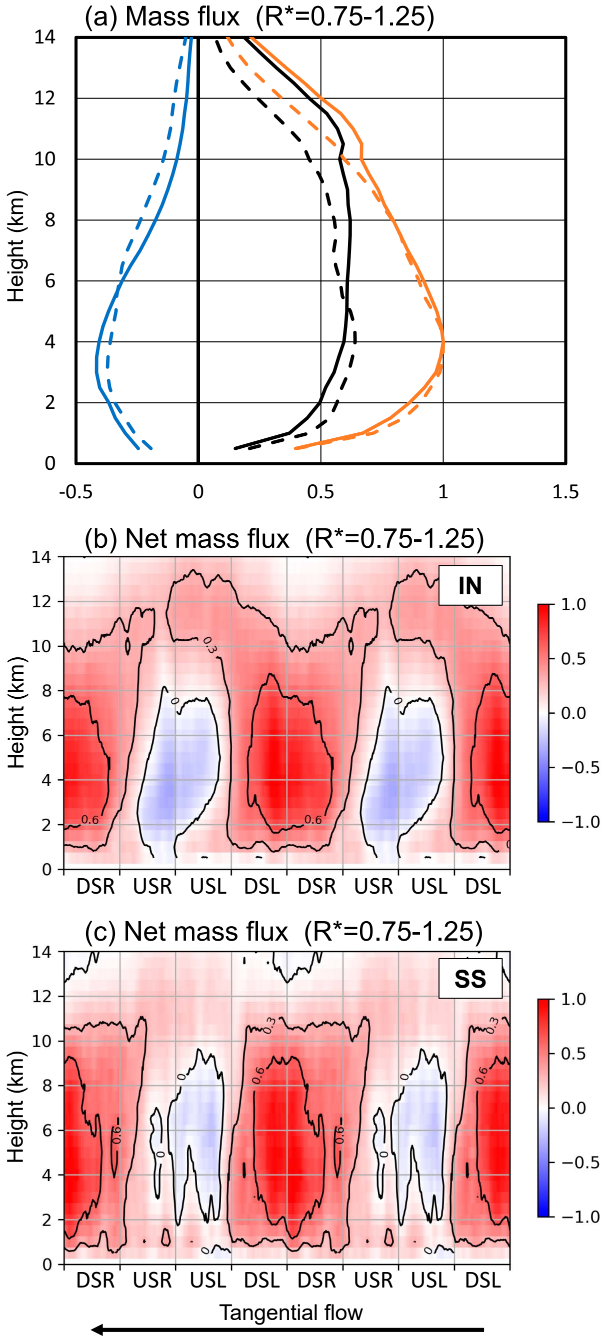

FIG. 11. (a) Vertical profiles of ascent (orange), descent (blue), and net (black) vertical mass flux in the eyewall region ($R^* = 0.75$–1.25) for IN (solid) and SS (dash) TCs normalized by the maximum ascent mass flux value (dimensionless). A small bump of ascent mass flux seen at 10-km height for IN cases is due to the difference in the quality control of w (section 2a). (b) Azimuth–height plot of net mass flux normalized by the maximum net mass flux value (colors) in the eyewall region ($R^* = 0.75$–1.25) for IN cases. The black contours denote 0, 0.3, and 0.6. The plots are extended to two revolutions. (c) As in (b), but for SS cases.

5. Discussion

Motivated by the analysis results of section 4, we briefly argue here possible factors and processes involved in the modulation of eyewall convection, including that in the USL upper-level region, and in the vertical development of the hurricane vortex, which may help to explain the differences in intensification rate between IN and SS cases. Given the limitations of airborne Doppler radar data and the composite approach (i.e., spatial and temporal coverage limitations, inability to measure thermodynamic fields), the discussion is confined to being mainly speculative regarding cause and effect. Further research, involving modeling studies and carefully constructed observational case studies, are required to adequately assess the mechanisms speculated here.

a. *Modulation of eyewall convection*

The higher frequency of moderate to strong updrafts USL at upper levels near $R^* = 1$ for IN cases implies that IN cases have greater buoyancy in the eyewall than SS cases (e.g., Zhang et al. 2000; Braun 2002; Eastin et al. 2005). As described in section 4a, SS cases include more cases with low OHC, strong vertical shear, or low midlevel humidity than IN cases. These factors may reduce buoyancy and limit eyewall convection (e.g., Riemer et al. 2010; Ge et al. 2013; Chen et al. 2021). Additionally, as noted in section 4b, six SS cases showed an outer symmetric tangential wind maximum consistent with the process of SEF. In such cases, outer organized convection may be a barrier to low-level inflow and modulate, or limit, eyewall convection (e.g., Zhou and Wang 2011; Bell et al. 2012; Didlake et al. 2017). As recently proposed by Smith et al. (2021), however, outer convection itself may be triggered by the low-level outflow arising from the inability of eyewall convection to ventilate mass exiting the boundary layer.

Another potential source of variability in eyewall convection is eye–eyewall mixing. The shear-relative vorticity anomalies and asymmetric flow pattern seen in the IN composite shown in section 4d are consistent with some previous studies that have argued the role of eye–eyewall mixing in the occurrence of vigorous convection (e.g., Braun and Wu 2007; Cram et al. 2007; Reasor et al. 2009; Guimond et al. 2016; Hazelton et al. 2017a). Cram et al. (2007) used a simulation of intensifying Hurricane Bonnie (1998) to demonstrate through a trajectory analysis that air transported from the low-level eye into the eyewall had positive buoyancy and that the majority of trajectories seeded in the eye were stirred out into the eyewall DSL. Enhanced USL upper-level ascent would then arise as a later stage of convection having rotated cyclonically downstream (DeHart et al. 2014). Further study is needed to examine whether such shear-relative mixing is important for hurricane intensification using a synthesis of the current TDR observations with additional thermodynamic observations along with modeling studies.

b. *Vertical development of the hurricane vortex*

In a recent study using TDR data, DesRosiers et al. (2023) demonstrated a statistically significant relationship between a

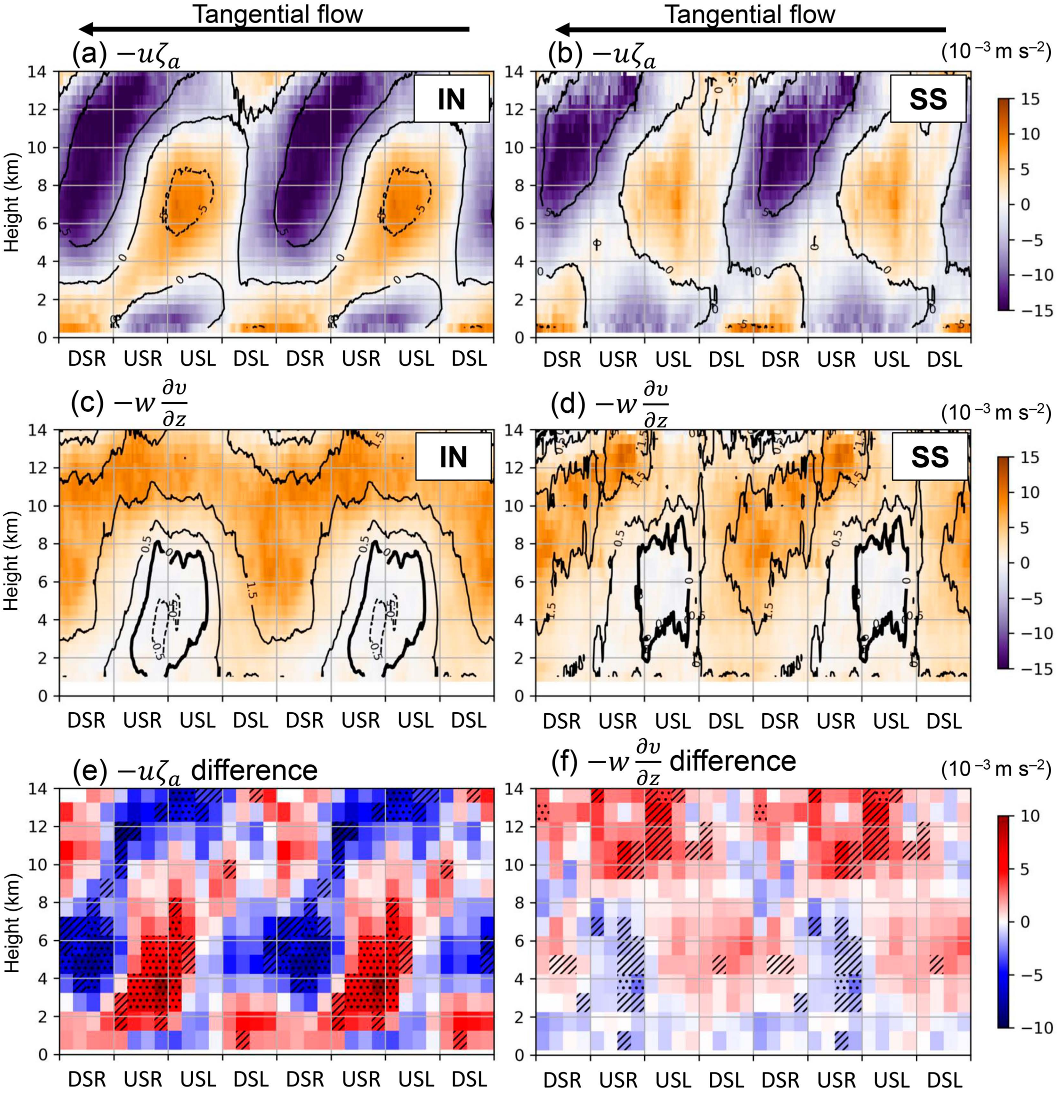

FIG. 12. Azimuth–height plots of the term $-u\zeta_a$ (colors; 10^{-3} m s^{-2}) and radial wind (contours; m s^{-1}) averaged over the eyewall region ($R^* = 0.75$–1.25) for (a) IN and (b) SS cases. The plots are extended to two revolutions. (c),(d) As in (a) and (b), but for the term $-w(\partial v/\partial z)$ (colors; 10^{-3} m s^{-2}) and vertical velocities (contours; m s^{-1}). (e),(f) Differences in $-u\zeta_a$ (10^{-3} m s^{-2}) and $-w(\partial v/\partial z)$ (10^{-3} m s^{-2}) between IN and SS cases (IN minus SS). Hatching indicates areas that are significant at the 95% significance level with a two-sided Wilcoxon–Mann–Whitney rank-sum test, and stippling indicates areas where p values pass an FDR test for field significance ($\alpha_{\mathrm{global}} = 0.05$). A minimum of 11 radial passes at any given location in azimuth–height space is required to make composite fields.

dynamic measure of TC height and future intensification, such that taller TCs (excluding major hurricanes, which are typically tall) tend to intensify at greater rates. In section 4e, it was shown that IN cases have a greater potential for vertical development of the vortex with the aid of strong USL upper-level ascent than SS cases, and thus would be expected to maintain, or even experience a strengthening of the vortex, at mid and upper levels following the observation period. Although the spinup of the maximum wind occurs in the boundary layer (e.g., Smith et al. 2009; Montgomery et al. 2014), vertical development of the vortex is favorable for continued intensification in shear environments. Riemer and Montgomery (2011) demonstrated that the degree to which a vortex may isolate itself from interactions with dry environmental air increases with vortex strength. If a vortex is shallow (i.e., a weak upper-level vortex), differential advection by environmental vertical shear can more easily bring mid- to upper-level dry air to the inner core of the vortex and lead to the suppression of deep convection (e.g., Alland et al. 2021; Fischer et al. 2023). A future study using analysis data referenced to the life cycle of eyewall convective events should examine how the vertical development of the hurricane vortex differs depending on the strength of USL ascent.

c. *Relationship to low-level intensification*

Whether convection is enhanced through eye–eyewall mixing or protected from negative environmental influences through vertical development of the vortex at mid and upper levels, ultimately deep convection over a sufficient fraction of the eyewall region is necessary for a net vertical mass flux strong enough to evacuate the air converging in the boundary layer and yield net inflow directly above the boundary layer (e.g., Smith et al. 2021). Figure 3b showed that this was indeed the case for IN cases. The inflow strengthens the vortex through the convergence of angular momentum above the boundary layer, which then contributes to further intensification of the maximum wind in the boundary layer (Smith and Montgomery 2015). This is essentially how we relate the more vigorous USL upper-level ascent observed in IN cases to the pertinent spinup mechanisms at lower levels. The inability to sustain such convection in the eyewall, whether it be due to upper-level warming and reduced convective instability as the storm approaches its maximum intensity, the eyewall becoming thermodynamically unfavorable through environmental interactions, or air emerging out of the boundary layer becoming less thermodynamically favorable through the development of organized convection at larger radii, requires further study to understand the SS subset of cases composited here.

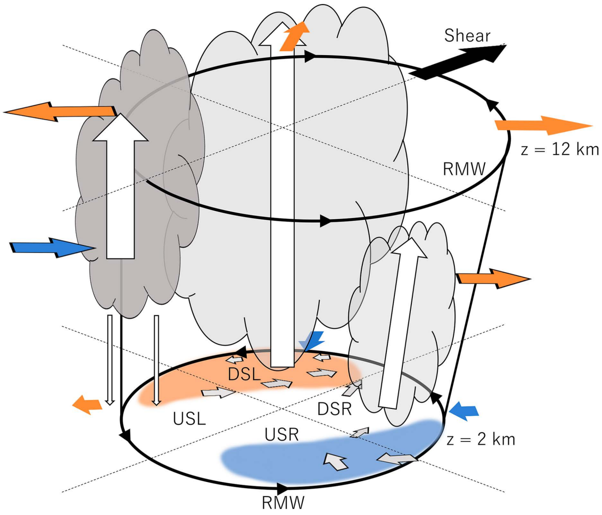

FIG. 13. Schematic diagram of shear-relative asymmetric characteristics of IN hurricanes. Black circles with arrows denote the RMWs at 2- and 12-km height. Blue and orange arrows denote representative quadrant-mean storm-relative inflow and outflow, respectively, with the black frame border indicating a statistically significant difference from SS cases. White arrows denote representative vertical velocities, and the cloud symbols denote higher frequencies of moderate to strong updrafts found in CFADs of IN hurricanes (Fig. 8). The light orange area represents a low-level positive vorticity anomaly, and the light blue area represents a low-level negative one. Gray arrows indicate the low-level asymmetric flow in the eye (Figs. 9a,b). The environmental vertical shear vector is indicated by the thick black arrow.

6. Conclusions

This study investigated differences in upshear-left (USL) ascent and other asymmetric kinematic characteristics between intensifying (IN) and steady-state (SS) hurricanes using airborne Doppler radar observations obtained from NOAA missions from 1997 to 2019. Figure 13 provides a schematic diagram of asymmetric characteristics for IN hurricanes in shear. Statistics from individual cases confirmed that more than 50% of IN cases have maximum wavenumber-1 (WN-1) ascent in the eyewall USL averaged at a height of 12 ± 0.5 km, whereas only 9% of SS cases do (Table 2). Strong ascent USL at upper levels can be a signal of ongoing intensification.

The shear-relative asymmetric structure of the composited eyewall for IN cases shows that eyewall ascent is strong not only in the USL quadrant at upper levels, but also in the convective initiation region in the down-shear right quadrant (DSR) (Fig. 4). The contoured frequency by altitude diagrams (CFADs) of vertical velocity indicate that IN cases have higher frequencies of moderate updrafts (2–6 m s^{-1}) in the downshear eyewall and moderate to strong updrafts (2–8 m s^{-1}) at 9–16-km heights USL than SS cases (Fig. 8). The vertical velocity characteristics of IN cases suggest that stronger convective cells that initiate DSR develop while rotating to the USL quadrant compared with SS cases. Composites of IN cases show that maximum WN-1 vorticity that tends to be located in the downshear-left quadrant (DSL) inside the RMW allows for low-level outflow from the eye to the downshear eyewall (Fig. 9) and strong convergence with low-level inflow associated with the vertical shear (Fig. 10), forming a stronger local secondary circulation downshear (Fig. 6). The vertical profile of mass flux shows that the vigorous eyewall convection of IN cases produces a net vertical mass flux increasing with height up to ~5 km and then is almost constant up to 10 km, whereas the net vertical mass flux of SS cases decreases with height above 4 km (Fig. 11). Although strong USL upper-level ascent does not directly drive low-level intensification, it provides greater potential for the vertical development of the hurricane vortex (Fig. 12), which is argued to be favorable for continued intensification in shear environments.

These findings have been partially documented by composite studies (Rogers et al. 2013; Wadler et al. 2018) and case studies (e.g., Zawislak et al. 2016; Rogers et al. 2016). This study provides a more complete, rigorous analysis of three-dimensional structural differences between IN and SS cases than Rogers et al. (2013) with an expanded database, including differences in low-level convergence downshear, eyewall ascent with the height of its peak strength increasing from DSR to USL, midlevel inflow upshear, and vertical advection of tangential wind USL. This study also found a significant difference in the upper-level ascent asymmetry between IN and SS cases that we have tied to the kinematic structure at lower levels, where recent intensification theories have focused on. We believe the findings of this study will lead to future work on how intensification occurs.

Some questions remain in this study. First, information on the boundary layer and thermodynamic conditions in the inner core is needed to evaluate the contribution of eye–eyewall mixing to vigorous eyewall convection from downshear to USL. Second, tail-Doppler radar analyses derived from observations collected over each IOP do not provide instantaneous snapshots of the kinematic field, which makes it difficult to conduct budget analyses and elucidate the role of detailed eddy processes in the development of eyewall convection. Third, this study has not considered the effect of storm size (i.e., the RMW) on the preference for USL ascent. The relationship between the azimuthal location of maximum WN-1 ascent and the RMW is not seen in the statistics from individual cases because the number of samples for both small and large storms is too small to examine (not shown). It may be possible, however, that the shear-relative distribution of convective updrafts differs between storms with RMWs of 10 and 50 km, for example. Performing idealized numerical simulations is a way to address these questions in future work.

Acknowledgments. The authors are grateful to the staff of NOAA aircraft missions. The authors thank John Gamache for his efforts in obtaining TDR analyses. The authors also thank anonymous reviewers for valuable comments that have greatly improved the manuscript. The idea of compositing the vertical velocity along the eyewall to look at the azimuthal asymmetries in the vertical velocity distributions relative to the shear vector (Fig. 4) is originally from the late Dr. Michael Black. This work was supported by a Fellowship Grant from the Ministry of Education, Culture, Sports, Science and Technology (MEXT) of the Japanese government, MEXT KAKENHI Grants 19K14797, 19H00705, 21H01164, and 23K13172. Jun Zhang was supported by Office of Naval Research Grant N00014-20-1-2071, NOAA Grants NA21OAR4590370 and NA22OAR4050669D, and National Science Foundation Grant AGS2211308.

Data availability statement. The swath TDR analysis data used in this study are contained within the TC-RADAR database, available at https://www.aoml.noaa.gov/ftp/pub/hrd/data/radar/level3/. The data used here are consistent with that in the current version v3k with swath type employing the original centering [i.e., not recentered following the methods in Fischer et al. (2022)]. In addition, SHIPS developmental data are available online at http://rammb.cira.colostate.edu/research/tropical_cyclones/ships/ (SHIPS 2020).

APPENDIX

Reflectivity Bias Correction

Discrepancies in reflectivity between the X-band Doppler radars installed on the P-3s (referred to as N42 and N43) exist due to calibration errors and can vary from year to year and, less frequently, within a season. This study adopts a probability matching method to correct the discrepancies between radars in a given season (but does not account for variations in calibration error from year to year). The method uses a cumulative distribution function (CDF) of reflectivity to adjust the reflectivity value of one radar to that of the other radar with the same probability in the CDF (e.g., Marks et al. 1993). Specifically, the following four steps are conducted: (i) to collect reflectivity data of a given TC that was observed in the inner core (a squared area of 200 km × 200 km centered at the TC center) by the two radars within 12 h, (ii) to calculate CDFs of reflectivity from the two radars at heights from 2 to 4 km (close to the flight level of the P-3s), (iii) to determine the correction value by averaging differences in the reflectivity at the 75th percentile between the two radars at heights from 2 to 4 km, and (iv) to add the correction value to reflectivity data observed by either radar to make lower reflectivities consistent with higher reflectivities. In step iii, the 75th percentile is used because it is not sensitive to outliers. Table A1 provides the correction values used in this study. The correction value in 2014 varies because the two radars were swapped between N42 and N43 during the season, resulting in different calibration errors. Bias correction is not performed for data in years when only one radar was used.

TABLE A1. Reflectivity bias correction. N42 and N43 are the names of the two aircraft that are equipped with one of the two radars. The correction row indicates that either radar reflectivity data observed by N42 or N43 should be corrected.

Year	Correction
1997	N43 + 9.5 dB = N42
2003	N43 + 1.6 dB = N42
2004	N43 + 4.0 dB = N42
2005	N43 = N42 + 3.6 dB
2007	N43 + 5.3 dB = N42
2008	N43 + 4.5 dB = N42
2009/10	N43 + 3.2 dB = N42
2012/13	N43 = N42 + 1.5 dB
2014, July	N43 = N42 + 2.8 dB
2014, early and mid-August	N43 = N42 + 5.8 dB
2014, after mid-August	N43 = N42 + 0.9 dB
2015–18	N43 = N42
2019	N43 + 6.4 dB = N42

REFERENCES

Alland, J. J., B. H. Tang, K. L. Corbosiero, and G. H. Bryan, 2021: Combined effects of midlevel dry air and vertical wind shear on tropical cyclone development. Part II: Radial ventilation. *J. Atmos. Sci.*, **78**, 783–796, https://doi.org/10.1175/JAS-D-20-0055.1.

Amrhein, V., S. Greenland, and B. McShane, 2019: Scientists rise up against statistical significance. *Nature*, **567**, 305–307, https://doi.org/10.1038/d41586-019-00857-9.

Bell, M. M., M. T. Montgomery, and W.-C. Lee, 2012: An axisymmetric view of concentric eyewall evolution in Hurricane Rita (2005). *J. Atmos. Sci.*, **69**, 2414–2432, https://doi.org/10.1175/JAS-D-11-0167.1.

Bender, M. A., 1997: The effect of relative flow on the asymmetric structure in the interior of hurricanes. *J. Atmos. Sci.*, **54**, 703–724, https://doi.org/10.1175/1520-0469(1997)054<0703:TEORFO>2.0.CO;2.

Beven, J. L., II, and D. Wroe, 2019: Tropical cyclone report: Hurricane Lane (15–28 August 2018). NHC Tech. Rep. EP142018, 28 pp., https://www.nhc.noaa.gov/data/tcr/EP142018_Lane.pdf.

Bister, M., and K. Emanuel, 2002: Low frequency variability of tropical cyclone potential intensity. 1. Interannual to interdecadal variability. *J. Geophys. Res.*, **107**, 4801, https://doi.org/10.1029/2001JD000776.

Black, M. L., J. F. Gamache, F. D. Marks Jr., C. E. Samsury, and H. E. Willoughby, 2002: Eastern Pacific Hurricanes Jimena of 1991 and Olivia of 1994: The effect of vertical shear on structure and intensity. *Mon. Wea. Rev.*, **130**, 2291–2312, https://doi.org/10.1175/1520-0493(2002)130<2291:EPHJOA>2.0.CO;2.

Braun, S. A., 2002: A cloud-resolving simulation of Hurricane Bob (1991): Storm structure and eyewall buoyancy. *Mon. Wea. Rev.*, **130**, 1573–1592, https://doi.org/10.1175/1520-0493(2002)130<1573:ACRSOH>2.0.CO;2.

——, and L. Wu, 2007: A numerical study of Hurricane Erin (2001). Part II: Shear and the organization of eyewall vertical motion. *Mon. Wea. Rev.*, **135**, 1179–1194, https://doi.org/10.1175/MWR3336.1.

——, M. T. Montgomery, and Z. Pu, 2006: High-resolution simulation of Hurricane Bonnie (1998). Part I: The organization of eyewall vertical motion. *J. Atmos. Sci.*, **63**, 19–42, https://doi.org/10.1175/JAS3598.1.

Cangialosi, J. P., A. S. Latto, and R. Berg, 2018: Tropical cyclone report: Hurricane Irma (30 August–12 September 2017). NHC Tech. Rep. AL112017, 111 pp., https://www.nhc.noaa.gov/data/tcr/AL112017_Irma.pdf.

Chen, S. S., J. A. Knaff, and F. D. Marks Jr., 2006: Effects of vertical wind shear and storm motion on tropical cyclone rainfall asymmetries deduced from TRMM. *Mon. Wea. Rev.*, **134**, 3190–3208, https://doi.org/10.1175/MWR3245.1.

Chen, X., J.-F. Gu, J. A. Zhang, F. D. Marks, R. F. Rogers, and J. J. Cione, 2021: Boundary layer recovery and precipitation symmetrization preceding rapid intensification of tropical cyclones under shear. *J. Atmos. Sci.*, **78**, 1523–1544, https://doi.org/10.1175/JAS-D-20-0252.1.

Cram, T. A., J. Persing, M. T. Montgomery, and S. A. Braun, 2007: A Lagrangian trajectory view on transport and mixing processes between the eye, eyewall, and environment using a high-resolution simulation of Hurricane Bonnie (1998). *J. Atmos. Sci.*, **64**, 1835–1856, https://doi.org/10.1175/JAS3921.1.

DeHart, J. C., R. A. Houze Jr., and R. F. Rogers, 2014: Quadrant distribution of tropical cyclone inner-core kinematics in relation to environmental shear. *J. Atmos. Sci.*, **71**, 2713–2732, https://doi.org/10.1175/JAS-D-13-0298.1.

DeMaria, M., and J. Kaplan, 1994: A Statistical Hurricane Intensity Prediction Scheme (SHIPS) for the Atlantic basin. *Wea. Forecasting*, **9**, 209–220, https://doi.org/10.1175/1520-0434(1994)009<0209:ASHIPS>2.0.CO;2.

——, and ——, 1999: An updated Statistical Hurricane Intensity Prediction Scheme (SHIPS) for the Atlantic and eastern North Pacific basins. *Wea. Forecasting*, **14**, 326–337, https://doi.org/10.1175/1520-0434(1999)014<0326:AUSHIP>2.0.CO;2.

——, M. Mainelli, L. K. Shay, J. A. Knaff, and J. Kaplan, 2005: Further improvements to the Statistical Hurricane Intensity Prediction Scheme (SHIPS). *Wea. Forecasting*, **20**, 531–543, https://doi.org/10.1175/WAF862.1.

DesRosiers, A. J., M. M. Bell, P. J. Klotzbach, M. S. Fischer, and P. D. Reasor, 2023: Observed relationships between tropical cyclone vortex height, intensity, and intensification rate. *Geophys. Res. Lett.*, **50**, e2022GL101877, https://doi.org/10.1029/2022GL101877.

Didlake, A. C., Jr., and R. A. Houze Jr., 2013: Dynamics of the stratiform sector of a tropical cyclone rainband. *J. Atmos. Sci.*, **70**, 1891–1911, https://doi.org/10.1175/JAS-D-12-0245.1.

——, G. M. Heymsfield, P. D. Reasor, and S. R. Guimond, 2017: Concentric eyewall asymmetries in Hurricane Gonzalo (2014) observed by airborne radar. *Mon. Wea. Rev.*, **145**, 729–749, https://doi.org/10.1175/MWR-D-16-0175.1.

Eastin, M. D., W. M. Gray, and P. G. Black, 2005: Buoyancy of convective vertical motions in the inner core of intense hurricanes. Part II: Case studies. *Mon. Wea. Rev.*, **133**, 209–227, https://doi.org/10.1175/MWR-2849.1.

Emanuel, K. A., 1986: An air-sea interaction theory for tropical cyclones. Part I: Steady-state maintenance. *J. Atmos. Sci.*, **43**, 585–605, https://doi.org/10.1175/1520-0469(1986)043<0585:AASITF>2.0.CO;2.

Fischer, M. S., P. D. Reasor, R. F. Rogers, and J. F. Gamache, 2022: An analysis of tropical cyclone vortex and convective characteristics in relation to storm intensity using a novel airborne Doppler radar database. *Mon. Wea. Rev.*, **150**, 2255–2278, https://doi.org/10.1175/MWR-D-21-0223.1.

——, ——, B. H. Tang, K. L. Corbosiero, R. D. Torn, and X. Chen, 2023: A tale of two vortex evolutions: Using a high-resolution ensemble to assess the impacts of ventilation on a tropical cyclone rapid intensification event. *Mon. Wea. Rev.*, **151**, 297–320, https://doi.org/10.1175/MWR-D-22-0037.1.

Frank, W. M., and E. A. Ritchie, 1999: Effects of environmental flow upon tropical cyclone structure. *Mon. Wea. Rev.*, **127**, 2044–2061, https://doi.org/10.1175/1520-0493(1999)127<2044:EOEFUT>2.0.CO;2.

——, and ——, 2001: Effects of vertical wind shear on the intensity and structure of numerically simulated hurricanes. *Mon. Wea. Rev.*, **129**, 2249–2269, https://doi.org/10.1175/1520-0493(2001)129<2249:EOVWSO>2.0.CO;2.

Ge, X., T. Li, and M. Peng, 2013: Effects of vertical shears and midlevel dry air on tropical cyclone developments. *J. Atmos. Sci.*, **70**, 3859–3875, https://doi.org/10.1175/JAS-D-13-066.1.

Guimond, S. R., G. M. Heymsfield, P. D. Reasor, and A. C. Didlake Jr., 2016: The rapid intensification of Hurricane Karl (2010): New remote sensing observations of convective bursts from the Global Hawk platform. *J. Atmos. Sci.*, **73**, 3617–3639, https://doi.org/10.1175/JAS-D-16-0026.1.

Hazelton, A. T., R. Rogers, and R. E. Hart, 2015: Shear-relative asymmetries in tropical cyclone eyewall slope. *Mon. Wea. Rev.*, **143**, 883–903, https://doi.org/10.1175/MWR-D-14-00122.1.

——, R. E. Hart, and R. F. Rogers, 2017a: Analyzing simulated convective bursts in two Atlantic hurricanes. Part I: Burst formation and development. *Mon. Wea. Rev.*, **145**, 3073–3094, https://doi.org/10.1175/MWR-D-16-0267.1.

——, ——, and ——, 2017b: Analyzing simulated convective bursts in two Atlantic hurricanes. Part II: Intensity change due to bursts. *Mon. Wea. Rev.*, **145**, 3095–3117, https://doi.org/10.1175/MWR-D-16-0268.1.

Hence, D. A., and R. A. Houze Jr., 2008: Kinematic structure of convective-scale elements in the rainbands of Hurricanes Katrina and Rita (2005). *J. Geophys. Res.*, **113**, D15108, https://doi.org/10.1029/2007JD009429.

——, and ——, 2011: Vertical structure of hurricane eyewalls as seen by the TRMM Precipitation Radar. *J. Atmos. Sci.*, **68**, 1637–1652, https://doi.org/10.1175/2011JAS3578.1.

Hendricks, E. A., S. A. Braun, J. L. Vigh, and J. B. Courtney, 2019: A summary of research advances in tropical cyclone intensity change from 2014–2018. *Trop. Cyclone Res. Rev.*, **8**, 219–225, https://doi.org/10.1016/j.tcrr.2020.01.002.

Heymsfield, G. M., J. B. Halverson, J. Simpson, L. Tian, and T. P. Bui, 2001: ER-2 Doppler radar (EDOP) investigations of the eyewall of Hurricane Bonnie during the Convection and Moisture Experiment-3. *J. Appl. Meteor.*, **40**, 1310–1330, https://doi.org/10.1175/1520-0450(2001)040<1310:EDRIOT>2.0.CO;2.

Houze, R. A., Jr., 1997: Stratiform precipitation in regions of convection: A meteorological paradox? *Bull. Amer. Meteor. Soc.*, **78**, 2179–2196, https://doi.org/10.1175/1520-0477(1997)078<2179:SPIROC>2.0.CO;2.

Huang, Y.-H., M. T. Montgomery, and C.-C. Wu, 2012: Concentric eyewall formation in Typhoon Sinlaku (2008). Part II: Axisymmetric dynamical processes. *J. Atmos. Sci.*, **69**, 662–674, https://doi.org/10.1175/JAS-D-11-0114.1.

Jordan, C. L., 1958: Mean soundings for the West Indies area. *J. Meteor.*, **15**, 91–97, https://doi.org/10.1175/1520-0469(1958)015<0091:MSFTWI>2.0.CO;2.

Kaplan, J., and M. DeMaria, 2003: Large-scale characteristics of rapidly intensifying tropical cyclones in the North Atlantic basin. *Wea. Forecasting*, **18**, 1093–1108, https://doi.org/10.1175/1520-0434(2003)018<1093:LCORIT>2.0.CO;2.

Kilroy, G., R. K. Smith, and M. T. Montgomery, 2016: Why do model tropical cyclones grow progressively in size and decay in intensity after reaching maturity? *J. Atmos. Sci.*, **73**, 487–503, https://doi.org/10.1175/JAS-D-15-0157.1.

Lonfat, M., F. D. Marks Jr., and S. Chen, 2004: Precipitation distribution in tropical cyclones using the Tropical Rainfall Measuring Mission (TRMM) Microwave Imager: A global perspective. *Mon. Wea. Rev.*, **132**, 1645–1660, https://doi.org/10.1175/1520-0493(2004)132<1645:PDITCU>2.0.CO;2.

Marks, F. D., Jr., R. A. Houze Jr., and J. F. Gamache, 1992: Dual-aircraft investigation of the inner core of Hurricane Norbert. Part I: Kinematic structure. *J. Atmos. Sci.*, **49**, 919–942, https://doi.org/10.1175/1520-0469(1992)049<0919:DAIOTI>2.0.CO;2.

——, D. Atlas, and P. T. Wills, 1993: Probability-matched reflectivity-rainfall relations for a hurricane from aircraft observations. *J. Appl. Meteor.*, **32**, 1134–1141, https://doi.org/10.1175/1520-0450(1993)032<1134:PMRRRF>2.0.CO;2.

Montgomery, M. T., and R. K. Smith, 2017: Recent developments in the fluid dynamics of tropical cyclones. *Annu. Rev. Fluid Mech.*, **49**, 541–574, https://doi.org/10.1146/annurev-fluid-010816-060022.

——, J. Zhang, and R. K. Smith, 2014: An analysis of the observed low-level structure of rapidly intensifying and mature Hurricane Earl (2010). *Quart. J. Roy. Meteor. Soc.*, **140**, 2132–2146, https://doi.org/10.1002/qj.2283.

Musgrave, K. D., R. K. Taft, J. L. Vigh, B. D. McNoldy, and W. H. Schubert, 2012: Time evolution of the intensity and size of tropical cyclones. *J. Adv. Model. Earth Syst.*, **4**, M08001, https://doi.org/10.1029/2011MS000104.

Nolan, D. S., Y. Moon, and D. P. Stern, 2007: Tropical cyclone intensification from asymmetric convection: Energetics and efficiency. *J. Atmos. Sci.*, **64**, 3377–3405, https://doi.org/10.1175/JAS3988.1.

Pendergrass, A. G., and H. E. Willoughby, 2009: Diabatically induced secondary flows in tropical cyclones. Part I: Quasi-steady forcing. *Mon. Wea. Rev.*, **137**, 805–821, https://doi.org/10.1175/2008MWR2657.1.

Reasor, P. D., M. D. Eastin, and J. F. Gamache, 2009: Rapidly intensifying Hurricane Guillermo (1997). Part I: Low-wavenumber structure and evolution. *Mon. Wea. Rev.*, **137**, 603–631, https://doi.org/10.1175/2008MWR2487.1.

——, R. Rogers, and S. Lorsolo, 2013: Environmental flow impacts on tropical cyclone structure diagnosed from airborne Doppler radar composites. *Mon. Wea. Rev.*, **141**, 2949–2969, https://doi.org/10.1175/MWR-D-12-00334.1.

Riemer, M., and M. T. Montgomery, 2011: Simple kinematic models for the environmental interaction of tropical cyclones in vertical wind shear. *Atmos. Chem. Phys.*, **11**, 9395–9414, https://doi.org/10.5194/acp-11-9395-2011.

——, ——, and M. E. Nicholls, 2010: A new paradigm for intensity modification of tropical cyclones: Thermodynamic impact of vertical wind shear on the inflow layer. *Atmos. Chem. Phys.*, **10**, 3163–3188, https://doi.org/10.5194/acp-10-3163-2010.

Rogers, R. F., P. Reasor, and S. Lorsolo, 2013: Airborne Doppler observations of the inner-core structural differences between intensifying and steady-state tropical cyclones. *Mon. Wea. Rev.*, **141**, 2970–2991, https://doi.org/10.1175/MWR-D-12-00357.1.

——, J. A. Zhang, J. Zawislak, H. Jiang, G. R. Alvey III, E. J. Zipser, and S. N. Stevenson, 2016: Observations of the structure and evolution of Hurricane Edouard (2014) during intensity change. Part II: Kinematic structure and the distribution of deep convection. *Mon. Wea. Rev.*, **144**, 3355–3376, https://doi.org/10.1175/MWR-D-16-0017.1.

——, P. D. Reasor, J. A. Zawislak, and L. T. Nguyen, 2020: Precipitation processes and vortex alignment during the intensification of a weak tropical cyclone in moderate vertical shear. *Mon. Wea. Rev.*, **148**, 1899–1929, https://doi.org/10.1175/MWR-D-19-0315.1.

Rozoff, C. M., D. S. Nolan, J. P. Kossin, F. Zhang, and J. Fang, 2012: The roles of an expanding wind field and inertial stability in tropical cyclone secondary eyewall formation. *J. Atmos. Sci.*, **69**, 2621–2643, https://doi.org/10.1175/JAS-D-11-0326.1.

Shimada, U., 2022: Variability of environmental conditions for tropical cyclone rapid intensification in the western North Pacific. *J. Climate*, **35**, 4437–4454, https://doi.org/10.1175/JCLI-D-21-0751.1.

SHIPS, 2020: Statistical tropical cyclone intensity forecast technique development: SHIPS developmental data. RAMMB, accessed 30 April 2020, https://rammb2.cira.colostate.edu/research/tropical-cyclones/ships/.

Sitkowski, M., J. P. Kossin, and C. M. Rozoff, 2011: Intensity and structure changes during hurricane eyewall replacement cycles. *Mon. Wea. Rev.*, **139**, 3829–3847, https://doi.org/10.1175/MWR-D-11-00034.1.

Smith, R. K., and M. T. Montgomery, 2015: Toward clarity on understanding tropical cyclone intensification. *J. Atmos. Sci.*, **72**, 3020–3031, https://doi.org/10.1175/JAS-D-15-0017.1.

——, and S. Wang, 2018: Axisymmetric balance dynamics of tropical cyclone intensification: Diabatic heating versus surface friction. *Quart. J. Roy. Meteor. Soc.*, **144**, 2350–2357, https://doi.org/10.1002/qj.3389.

——, M. T. Montgomery, and S. V. Nguyen, 2009: Tropical cyclone spin up revisited. *Quart. J. Roy. Meteor. Soc.*, **135**, 1321–1335, https://doi.org/10.1002/qj.428.

——, G. Kilroy, and M. T. Montgomery, 2021: Tropical cyclone life cycle in a three-dimensional numerical simulation. *Quart. J. Roy. Meteor. Soc.*, **147**, 3373–3393, https://doi.org/10.1002/qj.4133.

Stewart, S. R., 2004: Tropical cyclone report: Hurricane Ivan, 2–24 September 2004. NHC Tech. Rep., 44 pp., https://www.nhc.noaa.gov/data/tcr/AL092004_Ivan.pdf.

Tao, C., and H. Jiang, 2015: Distributions of shallow to very deep precipitation-convection in rapidly intensifying tropical cyclones. *J. Climate*, **28**, 8791–8824, https://doi.org/10.1175/JCLI-D-14-00448.1.

Vigh, J. L., J. A. Knaff, and W. H. Schubert, 2012: A climatology of hurricane eye formation. *Mon. Wea. Rev.*, **140**, 1405–1426, https://doi.org/10.1175/MWR-D-11-00108.1.

Wadler, J. B., R. F. Rogers, and P. D. Reasor, 2018: The relationship between spatial variations in the structure of convective bursts and tropical cyclone intensification as determined by airborne Doppler radar. *Mon. Wea. Rev.*, **146**, 761–780, https://doi.org/10.1175/MWR-D-17-0213.1.

Wilks, D. S., 2016: "The stippling shows statistically significant grid points." How research results are routinely overstated and overinterpreted, and what to do about it. *Bull. Amer. Meteor. Soc.*, **97**, 2263–2273, https://doi.org/10.1175/BAMS-D-15-00267.1.

Willoughby, H. E., and M. B. Chelmow, 1982: Objective determination of hurricane tracks from aircraft observations. *Mon. Wea. Rev.*, **110**, 1298–1305, https://doi.org/10.1175/1520-0493(1982)110<1298:ODOHTF>2.0.CO;2.

Wu, C.-C., Y.-H. Huang, and G.-Y. Lien, 2012: Concentric eyewall formation in Typhoon Sinlaku (2008). Part I: Assimilation of T-PARC data based on the ensemble Kalman filter (EnKF). *Mon. Wea. Rev.*, **140**, 506–527, https://doi.org/10.1175/MWR-D-11-00057.1.

Yuter, S. E., and R. A. Houze Jr., 1995: Three-dimensional kinematic and microphysical evolution of Florida cumulonimbus. Part II: Frequency distributions of vertical velocity, reflectivity, and differential reflectivity. *Mon. Wea. Rev.*, **123**, 1941–1963, https://doi.org/10.1175/1520-0493(1995)123<1941:TDKAME>2.0.CO;2.

Zawislak, J., H. Jiang, G. R. Alvey III, E. J. Zipser, R. F. Rogers, J. A. Zhang, and S. N. Stevenson, 2016: Observations of the structure and evolution of Hurricane Edouard (2014) during intensity change. Part I: Relationship between the thermodynamic structure and precipitation. *Mon. Wea. Rev.*, **144**, 3333–3354, https://doi.org/10.1175/MWR-D-16-0018.1.

Zelinsky, D. A., 2019: Tropical cyclone report: Hurricane Lorenzo (23 September–2 October 2019). NHC Tech. Rep. AL132019, 22 pp., https://www.nhc.noaa.gov/data/tcr/AL132019_Lorenzo.pdf.

Zhang, D.-L., Y. Liu, and M. K. Yau, 2000: A multiscale numerical study of Hurricane Andrew (1992). Part III: Dynamically induced vertical motion. *Mon. Wea. Rev.*, **128**, 3772–3788, https://doi.org/10.1175/1520-0493(2001)129<3772:AMNSOH>2.0.CO;2.

Zhang, J. A., R. F. Rogers, D. S. Nolan, and F. D. Marks Jr., 2011: On the characteristic height scales of the hurricane boundary layer. *Mon. Wea. Rev.*, **139**, 2523–2535, https://doi.org/10.1175/MWR-D-10-05017.1.

——, ——, P. D. Paul, and J. Gamache, 2023: The mean kinematic structure of the tropical cyclone boundary layer and its relationship to intensity change. *Mon. Wea. Rev.*, **151**, 63–84, https://doi.org/10.1175/MWR-D-21-0335.1.

Zhou, X., and B. Wang, 2011: Mechanism of concentric eyewall replacement cycles and associated intensity change. *J. Atmos. Sci.*, **68**, 972–988, https://doi.org/10.1175/2011JAS3575.1.